Journal of Controlled Release 334 (2021) 303–317

Contents lists available at ScienceDirect

Journal of Controlled Release

journal homepage: www.elsevier.com/locate/jconrel

Alendronate-functionalized hypoxia-responsive polymeric micelles for targeted therapy of bone metastatic prostate cancer

Mengmeng Long [a,1], Xuemeng Liu [a,1], Xu Huang [a], Min Lu [a], Xiaomei Wu [a], Lingyan Weng [a], Qiuping Chen [b], Xueting Wang [a,*], Li Zhu [a,*], Zhongping Chen [a,*]

[a] Institute of Special Environmental Medicine, Nantong University, Nantong, People's Republic of China
[b] Department of Anesthesiology, Affiliated Hospital of Nantong University, Nantong, People's Republic of China

ARTICLE INFO

Keywords:
Bone metastasis
Polymeric micelles
Alendronate
Bone-targeted delivery
Hypoxia-responsive release

ABSTRACT

Bone metastasis is one of the leading causes of cancer-related death and remains incurable in spite of great efforts. Bone-targeted nanoparticle-based drug carriers can overcome the difficulties in delivering therapeutic agents to metastatic bone and endowing them with a stimuli-responsive feature for controllable drug release can further maximize their therapeutic outcome. In light of hypoxic microenvironment of bone metastasis, we herein reported a bone-targeted and hypoxia-responsive polymeric micelle system for effective treatment of bone metastatic prostate cancer. The micelles were self-assembled from a polyethylene glycol and poly-L-lysine based copolymer using alendronate as a bone-targeted moiety and azobenzene as a hypoxia-responsive linker, showing a high affinity to metastatic bone and a high sensitivity in responding to hypoxia *in vitro*. *In vivo* studies further showed that after a selective accumulation in metastatic bone, the micelles could respond to hypoxic bone metastasis for rapid drug release to an effective therapeutic dosage. As a result, the micelles could suppress tumor growth in bone and inhibit bone destruction by inhibiting osteoclast activity and promoting osteoblast activity, achieving an enhanced therapeutic outcome with relieved bone pain and prolonged survival time. Bone-targeted and hypoxia-responsive nanocarriers therefore represent a promising advancement for treating bone metastasis. To our best knowledge, it might be the first example of the application of hypoxia-responsive nanocarriers in treating bone metastasis.

1. Introduction

Cancer metastasis is the leading cause of cancer-related death. Bone is one of the most common metastatic organs, as its physiological environments favor homing, survival, colonization, and further growth of metastatic cancer cells [1]. Bone metastasis has a high incidence in different cancer types, especially in prostate cancer, the second common cancer in over 50 years old men with more than 1 million newly diagnosed cases annually worldwide. Up to 65–90% of patients with prostate cancer and nearly all patients who die from prostate cancer display evidence of bone metastasis [2,3]. Patients with bone metastasis suffer from a series of skeletal complications such as intolerable pain, fracture, and hypercalcemia, which lead to increased morbidity, decreased quality of life, poor prognosis, and high mortality [4].

In spite of great progress in medical management by a multidisciplinary approach, bone metastasis remains incurable, due to its unique pathological and physiological characteristics. As the gold standard treatments, loco-regional radiotherapy and surgical resection fail to completely eliminate multiple nodules of bone metastasis and are often accompanied by a risk of bone-marrow suppression, hypocytosis, and even less life expectancy with aggravated pain. Conventional chemotherapy is the primary systemic treatment to suppress tumor growth; however, it is difficult for therapeutic agents to achieve an effective therapeutic dosage in metastatic bone *via* intravenous administration [5], due to the marrow-blood barrier and lack of specificity. Moreover, to acquire effective therapeutic magnitude in bone, therapeutic agents need to be administered at a high dosage and dosing frequency, which inevitably leads to dose-limiting side effects. The advancements in understanding the pathogenesis of bone metastasis shift treatment approaches from traditional chemotherapy to bone-targeted therapy, aiming at pain relief and fracture delay for improved quality of life. Among various bone-targeted agents targeting bone matrix or bone cells

* Corresponding author.
E-mail addresses: wangxueting@ntu.edu.cn (X. Wang), zhulizhou@ntu.edu.cn (L. Zhu), chenzp@ntu.edu.cn (Z. Chen).
[1] These authors contributed equally to this work

https://doi.org/10.1016/j.jconrel.2021.04.035
Received 14 January 2021; Received in revised form 20 April 2021; Accepted 27 April 2021
Available online 29 April 2021

(*e.g.*, osteoblasts, osteoclasts, and osteocytes) [6], nitrogen-containing bisphosphates (*e.g.*, alendronate, zoledronate, pamidronate, and olpadronate) are FDA-approved anti-resorptive agents clinically used to inhibit the activity of osteoclasts, due to their high affinity to bone, especially to cancer metastatic bone [7]. Unfortunately, they lack anti-tumor activity and have no improvement in overall survival, making them at best a palliative [2,8,9]. Moreover, high-dosage and long-term usage of bisphosphates also contributes to undesirable side effects such as bone turnover suppression, ocular dysfunction, and renal function impairment [10]. There is a need for continuous therapeutic development against bone metastasis.

Over the past decade, great efforts have been made to develop nanoparticle-based nanocarriers to overcome pharmacokinetic and pharmacodynamic drawbacks of therapeutic agents for improved drug accumulation at targeted sites [11]. Nowadays, substantial research has validated the effectiveness of nanocarriers in treating primary solid tumors; however, the difficulty in crossing the marrow-blood barrier still makes them not applicable for bone metastasis. Endowing nanocarriers with a bone-targeted effect is a promising modality to address this issue [12]. To this end, numerous bisphosphates-functionalized nanocarriers including liposomes, polymersomes/polymeric micelles, and inorganic nanoparticles have been designed [13]. Despite substantiated preferential accumulation in metastatic bone, many of bone-targeted nanocarriers show no significant survival improvement compared with non-targeted ones [14–17]. The failure in rapid drug release to an effective therapeutic dosage to suppress tumor growth in bone is one possible reason for their unsatisfactory therapeutic outcome. Stimuli-responsive nanocarriers triggered by bone metastasis microenvironments for spatiotemporally controllable drug release are thus highly demanded.

It has been reported that bone metastasis is inherently characterized by acidic pH, redox condition, specific enzymes (*e.g.*, cathepsin K, matrix metalloproteinases, and vacuolar H^+ ATPase), and local hyperthermia. In light of this, a series of pH-responsive, redox-responsive, enzyme-responsive, and thermo-responsive nanocarriers have been exploited to increase therapeutic dosage in metastatic bone [18]. Apart from aforementioned characteristics, hypoxia is also a hallmark of bone metastasis, potentiating metastatic tumor cell dormancy, micrometastasis formation, and its development in bone [19]. Although numerous hypoxia-responsive nanocarriers have been explored [20,21], their therapeutic outcome in treating bone metastasis has still not been addressed so far. Our previous findings revealed that hypoxia-responsive nanocarriers employing nitroaromatics or azobenzene (AZO) as hypoxia-responsive components could spontaneously respond to different types of hypoxic cells [22,23], showing the advantages in response sensitivity and universal applicability over other responsive systems. For example, acidic microenvironment occurs only after remarkable tumor growth or in osteolytic bone metastasis [24]; additional glutathione is needed to trigger the release of a redox-responsive system at cellular level [25]; the expression of a certain enzyme is variable in different cancer cell types and cancer progression stages, making enzyme-responsive nanocarriers not universally applicable [18]. Comparatively, hypoxia is a more realistic trigger since it is found in both bone marrow and bone metastatic nodules and is involved in lengthy process of bone metastasis [26]. Hypoxia-responsive nanocarriers are therefore supposed to be particularly valuable in therapeutic field of bone metastasis.

In this study, we attempt to fabricate bone-targeted and hypoxia-responsive polymeric micelles, self-assembled from a polyethylene glycol (PEG) and poly-L-lysine (PLL) based copolymer using alendronate (ALN) as a bone-targeted moiety and azobenzene (AZO) as a hypoxia-responsive linker, for effective treatment of bone metastatic prostate cancer based on our previous work [27]. The micelles are expected to be selectively accumulated in metastatic bone, facilitated by bone-targeted ALN in combination with the enhanced permeation and retention (EPR) effects; subsequently, they can respond to hypoxic bone metastasis for rapid payload release to an effective therapeutic dosage, facilitated by hypoxia-induced AZO cleavage for micelle disassembly. As a result, the micelles are capable of suppressing tumor growth in bone and inhibiting cancer-induced bone destruction and bone pain by balancing bone turnover, achieving a significant improvement in quality of life and overall survival (Scheme 1).

2. Materials and methods

2.1. Materials

Methoxy-polyethylene glycol-amine (mPEG-NH_2, M_w = 2000), carboxy-polyethylene glycol-amine (COOH-PEG-NH_2, M_w = 2000), and carboxy-polyethylene glycol-N-hydroxysuccinimide (HOOC-PEG-NHS, M_w = 2000) were purchased from ToYongBio Tech. Inc. (Shanghai, China). Sodium dithionite ($Na_2S_2O_4$), triphosgene, 4, 4′-azodiphenylamine, Nε-benzyloxycarbonyl-L-lysine (L-lysine CBZ), and alendronate (ALN) were obtained from J&K Scientific LTD (Beijing, China). Doxorubicin hydrochloride (DOX·HCl) was purchased from Meryer CO., LTD (Shanghai, China). N-hydroxysuccinimide (NHS) and 1-ethyl-3(3-dimethylpropylamine) carbodiimide (EDC) were acquired from Alfa Aesar (MA, USA). Near-infrared-emitting (NIR) fluorescent dye Cy5.5 was purchased from Lumiprobe corporation (FL, USA). Nicotinamide adenine dinucleotide (NADH) was purchased from Beyotime Biotechnology (Shanghai, China). All other chemicals were from Sinopharm Chemical Reagent CO., LTD. (Shanghai, China). Rat liver microsomes were obtained from the Research Institute for Liver Diseases (Shanghai, China). All reagents were of analytical grade and used as received. Millipore water was used in all experiments unless otherwise indicated.

For cell studies, mouse prostate cancer cell line (RM-1) was acquired from Cell Resource Center of Institute of Biological Sciences, Chinese Academy of Sciences (Shanghai, China). Fetal bovine serum (FBS), 0.25% trypsin-EDTA solution, and penicillin-streptomycin solution were purchased from Gibco Life Technologies (AG, Switzerland). Dulbecco's Modified Eagle's Medium (DMEM), 4′, 6-diamidino-2-phenylindole (DAPI), and 3-(4,5-dimethylthiazol-2-yl)-2,5-diphenyltetrazolium bromide (MTT) were obtained from Sigma (MO, USA). Anti-HIF-1α rabbit polyclonal antibody (No. ab228649) and its corresponding donkey anti-rabbit secondary antibody conjugated with Alexa Fluor® 555 nm (No. A31572) were purchased from Abcam (Cambridge, UK) and Thermo Fisher (MA, USA), respectively.

C57BL/6 mice (6-weeks old, 18–22 g in body weight, male) were supplied by Animal Center of Nantong University. The protocols for animal experiments were approved by Animal Care and Use Committee of Nantong University.

2.2. Synthetic procedures

2.2.1. Copolymer synthesis

Bone-targeted and hypoxia-responsive copolymer consisting of ALN, PEG, AZO, and PLL (ALN-PEG-AZO-PLL) was synthesized according to the literature with some modifications [28,29], as shown in Fig. 1. Briefly, ALN-PEG-AZO-PLL copolymer was synthesized *via* the following steps:1) synthesis of N-carboxy-(Nε-benzyloxycarbonyl)-L-lysine anhydride (L-lysine NCA) *via* the Fuchs–Farthing method using Nε-carbobenzyloxy-L-lysine (L-lysine CBZ) and triphosgene; 2) synthesis of COOH-PEG-AZO *via* the amide reaction of COOH-PEG-NHS with 4, 4′-azodiphenylamine; 3) synthesis of COOH-PEG-AZO-poly(Nε-benzyloxycarbonyl-L-lysine) (COOH-PEG-AZO-PBLL) *via* ring-opening polymerization initiated by amino terminal of COOH-PEG-AZO; 4) synthesis of ALN-PEG-AZO-PBLL *via* the amide reaction in the presence of EDC and NHS; 5) synthesis of ALN-PEG-AZO-PLL after removing amino-protecting benzyloxycarbonyl group from PBLL. Non-targeted and non-responsive mPEG-PLL and bone-targeted but non-responsive ALN-PEG-PLL were also synthesized for comparison. Detailed methods were described in the Supporting Information.

^{1}H NMR spectra of the copolymers were recorded on a 400 MHz NMR

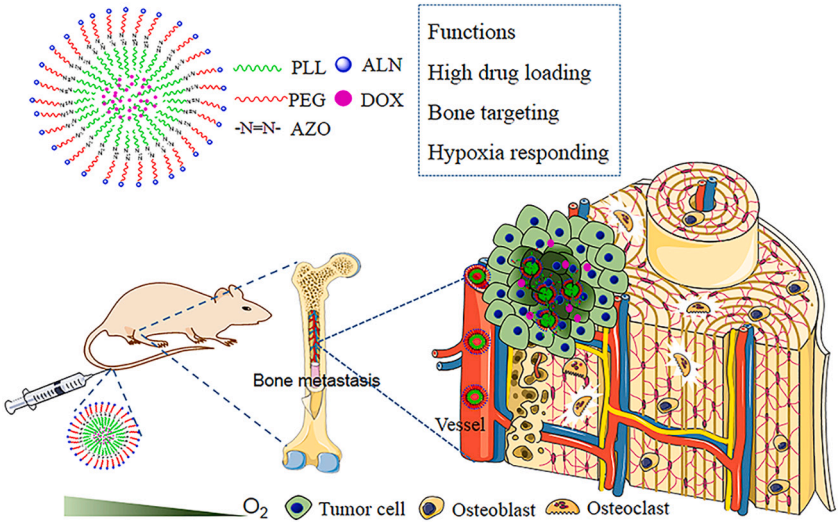

Scheme 1. Schematic illustration of ALN-functionalized hypoxia-responsive polymeric micelles for targeted therapy of bone metastatic prostate cancer.

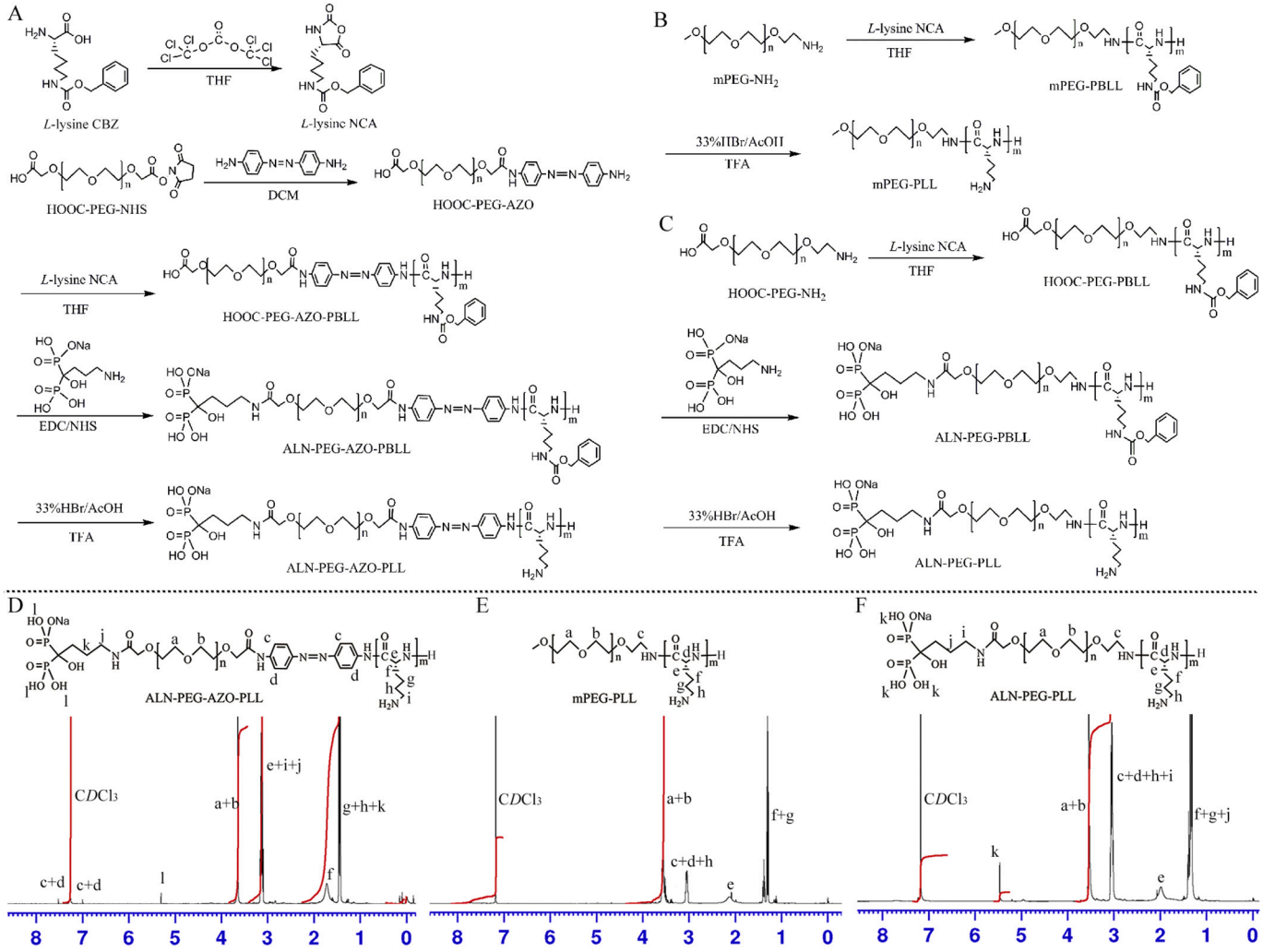

Fig. 1. Synthesis and characterization of the copolymers. Synthetic routes for (A) ALN-PEG-AZO-PLL, (B) mPEG-PLL, and (C) ALN-PEG-PLL. ^{1}H NMR spectra of (D) ALN-PEG-AZO-PLL, (E) mPEG-PLL, and (F) ALN-PEG-PLL.

spectrometer (Avance III , Bruker) using *CD*Cl$_3$ as the solvent. Gel permeation chromatography (GPC, CTO-20A, Shimadzu) was used to determine the molecular weight of the copolymers using dimethylformamide (DMF) as eluent and polystyrene as standard.

2.2.2. Preparation of blank and drug-loaded polymeric micelles

PEG-PLL, ALN-PEG-PLL, and ALN-PEG-AZO-PLL were employed to prepare conventional, bone-targeted, and bone-targeted and hypoxia-responsive polymeric micelles (denoted as PMs, ALN-PMs, and ALN-HR-PMs, respectively) *via* self-assembly technique. In a typical experiment for the synthesis of ALN-HR-PMs, 20 mg of ALN-PEG-AZO-PLL was dissolved in 4 mL of DMF, and 10 mL of water was added drop by drop with vigorous stirring. The mixture was then dialyzed against water (MWCO = 3000) for 24 h to obtain micelle suspension. ALN-HR-PMs were collected after freeze-drying for further use.

To prepare DOX-loaded micelles (PMs/DOX, ALN-PMs/DOX, and ALN-HR-PMs/DOX), DOX·HCl was firstly desalted (Supporting Information) and thereafter mixed with the copolymer in DMF for micelle preparation according to the above-described protocol. Cy5.5-loaded micelles (PMs/Cy5.5, ALN-PMs/Cy5.5, and ALN-HR-PMs/Cy5.5) were synthesized using the same protocol for NIR fluorescence imaging. The ratio of DOX to copolymer was 4:20 (w/w) for DOX loading, while it was 0.1/20 (w/w) for Cy5.5 loading.

2.3. Micelle characterization

2.3.1. Size, surface charge, morphology, and drug loading

The size and morphology of the micelles were observed on a transmission electron microscope (TEM, JEM-1230, Japan). The micelles were dropped on copper grids and then stained with 1% phosphotungstic acid solution (w/v) before observation. Hydrodynamic diameter, polydispersity index (PDI), and zeta potential of the micelles were investigated by dynamic light scattering technique (DLS, Zetasizer ZS90, Malvern). To determine drug loading efficiency (DLE, %) and drug loading capacity (DLC, %) of the micelles, 200 μL of DOX-loaded micelle suspension (10 mg of the micelles dispersed in 10 mL of water) was added into 4.8 mL of methanol solution. After sonication for 5 min (10 s on and 10 s off) with an ultrasonic cell pulverizer (JY92-2D, Zhejiang Xinzhi Biotech, China) to completely rupture the micelles, the mixture was centrifuged at 10000 rpm for 10 min and the supernatant with loaded DOX was collected. A high-performance liquid chromatography (HPLC, Waters) system equipped with a separation module (Waters e2695) and a fluorescence detector (2475 FLR Detector) was used to quantitatively analyze DOX based on a pre-established standard curve. HPLC conditions were as follows: column, ultimate® AQ-C18 (4.6 × 250 mm, 5 μm); mobile phase, methanol/acetonitrile/0.02 mM ammonium phosphate/glacial acetic acid (52:5:43:6, v/v); flow rate, 1 mL/min; column temperature, 30 °C; injection volume, 20 μL; fluorescence detector, 488 nm in excitation wavelength and 555 nm in emission wavelength. A standard curve was constructed by plotting peak area as a function of DOX concentrations ranging from 20 to 100 μg/mL ($y = 657.2\times - 531.4$, $R^2 = 0.9992$). DLE was defined as the weight of loaded DOX relative to the weight of initially added DOX, while DLC was defined as the weight of loaded DOX relative to the weight of initially added DOX and copolymers.

2.3.2. In vitro response to hypoxia

A chemical hypoxia (2 mg of $Na_2S_2O_4$ in 2 mL of water) and a biological hypoxia (20 μL of rat liver microsomes and 2 mg of NADH in 2 mL of pH 7.4 PBS) were generated, respectively, to mimic hypoxic bone metastasis microenvironment. Subsequently, 2 mg of the micelles were added into above solution and sealed in a quartz cuvette for 12 h. The changes in characteristic peaks before and after hypoxia treatment were recorded to study *in vitro* response to hypoxia on a UV–vis spectrophotometer (UV-2401PC, Shimadzu). AZO and the copolymers were also treated for comparison.

2.3.3. In vitro hypoxia-responsive drug release

While $Na_2S_2O_4$ would quench DOX fluorescence, *in vitro* hypoxia-triggered drug release was carried out in the biological hypoxia. Briefly, in a dialysis bag (MWCO = 3000), 10 mg of DOX-loaded micelles with 100 μL of rat liver microsomes and 10 mg of NADH was dispersed in 10 mL of degassed PBS (pH 7.4). The dialysis bag was then dialyzed against 30 mL of degassed PBS (pH 7.4) with gentle shaking at 37 °C. Degassing was performed throughout the study to maintain hypoxic condition. At predetermined intervals (0.5, 1, 2, 4, 6, 12 and 24 h), 0.5 mL aliquot of the dialysate was withdrawn for DOX quantification using HPLC. Equivalent fresh PBS was added immediately when the dialysate was withdrawn. The micelles alone were studied as a normoxic control. The cumulative release (%) defined as the total released DOX at predetermined intervals relative to the initial loaded DOX was finally plotted *versus* time.

2.3.4. In vitro bone-targeted efficiency

The binding efficiency of ALN-functionalized micelles to hydroxyapatite (HA) was studied to assess bone-targeted efficiency according to a previous work [30]. Typically, 3 mg of ALN-HR-PMs/DOX or non-targeted PMs/DOX were dispersed in 10 mL of water, followed by addition of 500 mg of HA. The mixture was gently shaken and 200 μL aliquot of the mixture was withdrawn at predetermined intervals (0.5, 1, 2, 3, and 4 h,). After centrifugation at 3000 rpm for 10 min, the supernatant containing unbound micelles was separated and treated with 4.8 mL of methanol for DOX quantification based on the procedure described in Section 2.3.1. The binding efficiency was calculated according to the following formula:

Binding efficiency (%) = (1-unbound DOX/loaded DOX) × 100%.

2.4. Cell experiments

2.4.1. Cell culture

RM-1 cells were cultured in DMEM medium (37 °C, 5% CO_2, 21% O_2) containing 1% penicillin/streptomycin antibiotic and 10% FBS. The culture medium was refreshed every 1–2 days and the cells were passaged when reaching approximately 80% confluence.

2.4.2. Hypoxia-responsive intracellular release

To concretely observe hypoxia-responsive drug release, RM-1 cells (2×10^4 cells per dish) were seeded in a polystyrene/glass confocal dish (No. BDD011035, JET BIOFIL) and cultured for 24 h. After treatment with different drug formulations at 10 μg/mL of DOX concentration for 2 h followed by washing with PBS (pH 7.4) to remove drug-containing medium, a φ14 mm coverslip was put on the cells cultured on the glass bottom of confocal dish to create a decreasing oxygen concentration from its edge to the center [22,31,32]. After another 3 h incubation, DOX fluorescence of the cells was observed on a confocal laser scanning microscope (CLSM, TCS SP8, Leica) (488 nm laser and 590 ± 10 nm emission filter for DOX).

To study hypoxia-responsive drug release in the fixed hypoxic conditions, RM-1 cells were seeded in a glass-bottom culture dish (2×10^5 cells per dish) and cultured for 24 h. Afterwards, the cells were treated with different drug formulations at 10 μg/mL of DOX concentration for 2 h and washed twice with PBS (pH 7.4). The cells were then divided into two groups. One group was sequentially cultured under normoxic condition (21% O_2), while the other was cultured under hypoxic condition (1% O_2) using a hypoxia incubator (INVIVO2, Ruskinn). Three hours later, all cells were washed with PBS (pH 7.4) twice and stained with DAPI. The fluorescence of the cells was observed on the CLSM in two channels relevant to DAPI and DOX.

Flow cytometry was further used to quantitatively analyze hypoxia-responsive intracellular release of DOX. RM-1 cells were cultured in a petri dish, treated with different drug formulations for 2 h, washed with PBS (pH 7.4), and further cultured under normoxic or hypoxic conditions for 3 h, as described above. In the following, the cells were collected through trypsinization and centrifugation and re-suspended in PBS (pH 7.4) with cell intensity not less than 1×10^6 cells/mL. The red fluorescence of DOX in FL2 gate (575 nm) was then detected and quantified on a flow cytometer (Gallios, Beckman Coulter) using 488 nm

laser.

2.4.3. Cell migration

Cell migration was assessed by wound healing assay. RM-1 cells (2×10^4 cells per well) were seeded in 6-well plates, cultured for 24 h, and treated with different drug formulations at 10 μg/mL of DOX concentration for 2 h. After removing drug-containing medium, a 10 μL pipette tip was used to generate a wound area by scraping cell monolayer. The cells were then incubated under normoxic or hypoxic conditions for 24 h. The wound width was observed and recorded on an inverted microscope. The migration ratio was defined as follows:

Migration ratio (%) = $(A_0 - A_i) / A_0 \times 100$.

Where A_i and A_0 were the remaining area of the region without cells after treatment and the initial area before treatment, respectively. The area of the selected region was analyzed by Image J software.

2.4.4. Cytotoxicity

In vitro cytotoxicity was assessed by MTT assay. RM-1 cells seeded in 96-well plates (3000 cells per well) were cultured and treated with different drug formulation for 2 h. After removing drug-containing medium, the cells were cultured under normoxic or hypoxic conditions for 48 h. The cells were then washed with PBS (pH 7.4) and treated for MTT assay using an automatic microplate reader (SN209941, Bio-TEK) at 570 nm.

2.5. Animal experiments

2.5.1. Murine model of bone metastatic prostate cancer

RM-1 cell suspension of PBS (pH 7.4) (5×10^7 cells/mL) was placed on ice for use. After anesthetization with 5% chloral hydrate by intraperitoneal injection, the femur of the right hind limb of the mice was exposed carefully by surgery. Then, 20 μL of above-prepared cell suspension was carefully injected into the femur with a 29-gauge needle and subsequently, the pinhole was sealed with bone wax. The mice after modeling were given food and water freely.

2.5.2. Pharmacokinetics and tissue distribution

Pharmacokinetic study was performed in healthy C57BL/6 mice. The mice were intravenously injected with different drug formulations at equivalent DOX dosage (5 mg/kg body weight). At predetermined intervals (0.05, 0.25, 0.5, 1, 2, 4, 12 and 24 h), the mice were euthanized, and 0.5 mL of blood was taken from mouse orbital. The blood was centrifuged at 8000 rpm for 10 min and the collected plasma was mixed with 3 mL of chloroform and methanol (4:1, v/v). The mixed plasma was vortex for 5 min and centrifuged at 8000 rpm for 10 min to collect extracted DOX in the upper chloroform layer. After evaporating chloroform, 3 mL of methanol was added into the samples to completely precipitate plasma protein, followed by centrifugation at 8000 rpm for another 10 min. The methanol layer containing DOX was collected and filtered with syringe filter (0.45 μm in pore diameter). Finally, 20 μL of obtained methanol solution was injected into HPLC for DOX quantification.

Tissue distribution was assessed in tumor-bearing C57BL/6 mice. On the 7th day after modeling, tumor-bearing mice were intravenously injected with different drug formulations at equivalent DOX dosage (5 mg/kg body weight). At predetermined intervals (1 and 12 h), the mice were euthanized for prefusion-fixation and the tissues of heart, liver, spleen, lung, kidney, metastatic bone, and contralateral tumor-free bone were then harvested. Following tissue homogenization using a homogenizer (FastPrep-24TM 5G, Shanghai Boyi Biotech, China), the samples were treated with 5 mL of chloroform and methanol (4:1, v/v) for DOX qualification according to the protocol used for blood sample preparation.

2.5.3. In vivo NIR imaging

On the 7th day after modeling, tumor-bearing mice were intravenously injected with different Cy5.5-loaded formulations at equivalent Cy5.5. NIR fluorescence images were acquired and presented in visible pseudo-color mode at predetermined intervals (0.5, 1, 2, 4, 6, 12, and 24 h) using a small animal dedicated IVIS imaging system (Lumina II, Caliper Life Sciences), and fluorescence intensity was analyzed by IVIS imaging software. Following the last imaging at 24 h, the mice were euthanized, and the tissues of heart, liver, spleen, lung, kidney, metastatic bone, and contralateral tumor-free bone were harvested for *ex vivo* imaging. Default illumination settings of Cy5.5 filter were used for imaging throughout the whole study.

2.5.4. Immunofluorescence staining

Following *ex vivo* NIR imaging at 24 h post-injection, tumor tissue was stripped from the harvested metastatic bone, followed by dehydration and transparentization for paraffin sectioning. The obtained slices were rehydrated and sequentially incubated with anti-HIF-1α rabbit polyclonal antibody (1:250) overnight at 4 °C, its corresponding donkey anti-rabbit fluorescence-conjugated secondary antibody conjugated with Alexa Fluor® 555 nm (1:800) at room temperature for 1 h, and DAPI for 8 min. After rinsing with PBS (pH 7.4) and covering with a coverslip, the fluorescence of DAPI, HIF-1α, and Cy5.5 was observed using their corresponding fluorescence filters on the CLSM.

2.5.5. Pain-related behavior evaluation

On the 7th day after modeling, tumor-bearing mice were intravenously injected with different drug formulations at equivalent DOX dosage (5 mg/kg body weight) every four days. The mice treated with PBS (pH 7.4) were studied as a control group. Pain-related behaviors such as number of flinches, spontaneous lifting time, and movement scores of tumor-bearing limb were measured during a 4-min period according to our previous work [27]. The mice were acclimated in a glass box for 10 min before measurement and pain-related behavior evaluation started from the 1st day after modeling. Meanwhile, the survival of the mice was checked every day.

2.5.6. Micro-computed tomography (micro-CT) imaging

On the 21st day after modeling, the mice were euthanized and metastatic bone was harvested for Micro-CT two-dimensional (2D) scanning on a Micro-CT (SKYSCAN 1176, Bruker, Belgium). Following three-dimensional (3D) reconstruction, bone analysis software was used to evaluate bone mineral density (BMD) and trabecular bone number (Tb.N). Healthy bone from healthy mice was also scanned as a control.

2.5.7. Bone staining

Hematoxylin and eosin (H&E), tartrate-resistant acid phosphatase (TRAP), alkaline phosphatase (ALP) and TRAP/ALP staining of metastatic, tumor-free, and healthy bone were performed to further assess the therapeutic outcome of different drug formulations. Bone decalcification was necessary before prepared into slice for staining. Typically, the harvested metastatic bone from the mice euthanized on the 21st day after modeling was put into periodate-*L*-lysine-paraformaldehyde (PLP) solution for 24 h for fixing. After terminating fixing using PBS (pH 7.4), the samples were placed into 5% glycerol-PBS, 10% glycerol-PBS, and 15% glycerol-PBS solutions, respectively, for 12 h at 4 °C for rinsing. Subsequently, the samples were transferred to ethylenediaminetetraacetic acid (EDTA)-glycerol solution for 10–15 days at 4 °C for decalcification. The decalcification process was observed under the microscope. The decalcified samples were then immersed in 15% sucrose-7.5% glycerol-PBS, 15% sucrose-PBS, 7.5% sucrose-PBS, and PBS (pH 7.4) solutions, respectively, for 12 h at 4 °C for rinsing. Finally, the samples were dehydrated with graded ethanol, transparentized with xylene, embedded in paraffin, and sectioned into 6 μm slices for H&E staining or TRAP, ALP, and TRAP/ALP staining using TRAP/ALP staining kit® (Wako, Osaka, Japan), based on the supplier's recommended protocol.

2.5.8. Safety assessment

On the 21st day after modeling, the tissues of heart, liver, spleen, lung, and kidney were harvested from the mice euthanized for bone staining. After paraffin sectioning, histopathological examination of the tissues was carried out by H&E staining.

2.6. Data analysis

All data were analyzed by GraphPad Prim 7 software and statistically compared using unpaired student's *t*-test for two groups or one-way analysis of variance (ANOVA) test for multiple groups. A *p*-value less than 0.05 ($p < 0.05$) was defined as a statistically significant difference.

3. Results and discussion

3.1. Synthesis and characterization of the micelles, in vitro response to hypoxia, and bone-targeted efficiency

To fabricate ALN-HR-PMs, we firstly synthesized amphiphilic ALN-PEG-AZO-PLL copolymer composed of ALN as bone-targeted moiety, PEG and PLL as hydrophilic and hydrophobic blocks, respectively, and AZO as hypoxia-responsive linker of PEG and PLL. Heterobifunctional HOOC-PEG-NHS was utilized as starting material, NHS terminal of which was conjugated with AZO. The residual amino terminal of AZO initiated ring-opening polymerization of L-lysine NCA for the formation of amino-protected PLL. After conjugation with ALN using carboxyl terminal of PEG followed by amino-protecting group removal, ALN-PEG-AZO-PLL was obtained (Fig. 1A). PEG-PLL and ALN-PEG-PLL were also synthesized based on the similar procedures (Fig. 1B and C). M_w values of obtained PEG-PLL, ALN-PEG-PLL, and ALN-PEG-AZO-PLL were 6278, 6770, and 7074, respectively, as determined by GPC (supplementary Fig. S1). Three copolymers had a low PDI($M_w/M_n < 1.2$) with the degree of polymerization around 29 for PEG-PLL and 31 for ALN-PEG-PLL and ALN-PEG-AZO-PLL. ^{1}H NMR results confirmed the successful synthesis of three copolymers. ALN-PEG-AZO-PLL showed characteristic peaks at 6.96 and 7.53 ppm from AZO and at 5.32 ppm from ALN, differentiating it from PEG-PLL and ALN-PEG-PLL (Fig. 1D-1F and supplementary Fig. S2).

Due to its amphiphilic nature, ALN-PEG-AZO-PLL as well as PEG-PLL and ALN-PEG-PLL could self-assemble in aqueous condition to form ALN-HR-PMs as well as PMs and ALN-PMs. PMs, ALN-PMs, and ALN-HR-PMs showed 169.1 nm, 175.7 nm, and 186.2 nm in hydrodynamic diameter, while their zeta potential was 43.5 mV, 36.7 mV, 35.3 mV, respectively, as determined by DLS (Supplementary Table S1 and Fig. S3). ALN conjugation led to the relatively large size of ALN-PMs compared with PMs, and AZO insertion further contributed to the size increase of ALN-HR-PMs. Positive surface charge of the micelles was owing to PLL with abundant amino groups, which was slightly reduced after ALN conjugation. The size of nanoparticles plays a vital role in drug delivery to tumor. It has been reported that nanoparticles of 100–200 nm in diameter can effectively escape renal filtration to remain in blood circulation system [33], further favoring their extravasation from circulation system into metastatic bone [34]. Thus, ALN-HR-PMs as well as PMs and ALN-PMs show a suitable size for effective drug delivery to bone metastasis. In the following, DOX as a model anticancer drug was loaded into the micelles to form PMs/DOX, ALN-PMs/DOX, and ALN-HR-PMs/DOX. At the fixed ratio of DOX to copolymer (4:20, w/w), obtained micelles exhibited high DLE and DLC. As demonstrated in supplementary Table S1, DLE of PMs/DOX, ALN-PMs/DOX, and ALN-HR-PMs/DOX was 69.3%, 75.1%, and 87.1%, while their DLC was 13.9%, 15.0%, and 17.4%, respectively. The higher DLE of ALN-PMs/DOX than PMs/DOX indicated that ALN conjugation facilitated the adsorption of DOX onto the surface of the micelles. Meanwhile, rigid AZO provided more inner space for DOX loading and ALN-HR-PMs/DOX thus showed higher DLE and DLC than ALN-PMs/DOX. It could also be found that DOX loading had a slight effect on the surface charge of the micelles and played a considerable role in their size. The size determined by DLS technique is calculated from the fluctuations of scattered light intensity due to the Brownian movement of nanoparticles and the large and heavy nanoparticles move slowly in comparison to the small and light ones [35]. After loading substantial DOX, the Brownian movement of the micelles decreases, leading to the increase of calculated size. Moreover, DOX adsorbed onto the surface of the micelles also contributed to the size increase.

We next studied the response of the micelles to hypoxic conditions generated by $Na_2S_2O_4$ and liver microsomes/NADH, respectively. $Na_2S_2O_4$ is a classic deoxidizer [36], which can rapidly reduce oxygen concentration to zero (Supplementary Fig. S4), while liver microsomes can induce some redox reactions to mimic *in vivo* hypoxic conditions when cooperating with NADH [37]. When exposed to either $Na_2S_2O_4$ or liver microsomes/NADH, AZO in ALN-HR-PMs will undergo rapid reductive cleavage, triggering the disassembly of ALN-HR-PMs for drug release (Fig. 2A). Hypoxia-induced AZO cleavage in ALN-HR-PMs was validated by UV–vis spectra. ALN-HR-PMs showed two characteristic peaks at 392 and 430 nm (Fig. 2B), originating from AZO (Supplementary Fig. S5); after hypoxic treatment, these two peaks disappeared, indicating AZO cleavage. In contrast, PMs and ALN-PMs showed no difference before and after hypoxic treatment (Fig. 2C and D). The disassembly of ALN-HR-PMs, triggered by hypoxia-induced AZO cleavage, was further confirmed by TEM observation. As revealed in Fig. 2E, ALN-HR-PMs as well as PMs and ALN-PMs were of regular spherical structure; once exposed to hypoxia, intact ALN-HR-PMs were cleaved and no regular structure was observed. In contrast, no change was found in PMs and ALN-PMs. It was worth noting that TEM size of three micelles was approximate (less than 100 nm), which was significantly smaller than DLS size. The sample prepared for TEM needs dehydration and immobilization, leading to its size always smaller than that in solvent-swollen state for DLS [38]. The disassembly of ALN-HR-PMs was supposed to accelerate the release of their payload, as validated by the cumulative release profiles of the micelles. As depicted in Fig. 2F, PMs/DOX and ALN-PMs/DOX exhibited similar drug release kinetics with less than 30% of loaded DOX released in 24 h, regardless of normoxia or hypoxia. This slight release should be attributed to DOX adsorbed onto the surface of the micelles. Although DOX released from ALN-HR-PMs/DOX under normoxic condition was equivalent to that from PMs/DOX and ALN-PMs/DOX, more than 40% of loaded DOX was released under hypoxic condition in 1 h and more than 70% was released in 24 h. The release of ALN-HR-PMs/DOX was dramatically accelerated under hypoxic condition, indicating their high sensitivity to hypoxia.

Hydroxyapatite (HA) is the main inorganic component in bone. Hydroxyl and phosphonate groups of ALN have a high affinity to HA [15] and *in vitro* bone-targeted efficiency of ALN was thus evaluated by studying its binding with HA. After mixing ALN-HR-PMs/DOX dispersed in water with water-insoluble HA, the solution became clear and red ALN-HR-PMs/DOX almost completely precipitated, indicating their specific binding with HA. Comparatively, the solution with mixed PMs/DOX remained red, although some red precipitates were observed, due to non-specific adsorption (Fig. 2H). The binding rate was further quantified and as shown in Fig. 2G, up to 96% of ALN-HR-PMs/DOX was bound to HA in 4 h, while only 25% of ALN-free PMs/DOX was bound. This result indicated that ALN-HR-PMs/DOX had a strong affinity to bone for bone-targeted drug delivery.

3.2. Hypoxia-responsive intracellular drug release for improved anticancer efficacy in vitro

The therapeutic outcome of nanoparticles as drug carriers is highly associated with their uptake by cells and subsequent drug release. We firstly studied hypoxia-responsive drug release by covering a glass coverslip on the cultured cells, where a non-quantitative gradient hypoxia was generated with the oxygen concentration decreasing from the edge to center of the coverslip. CLSM images showed that the

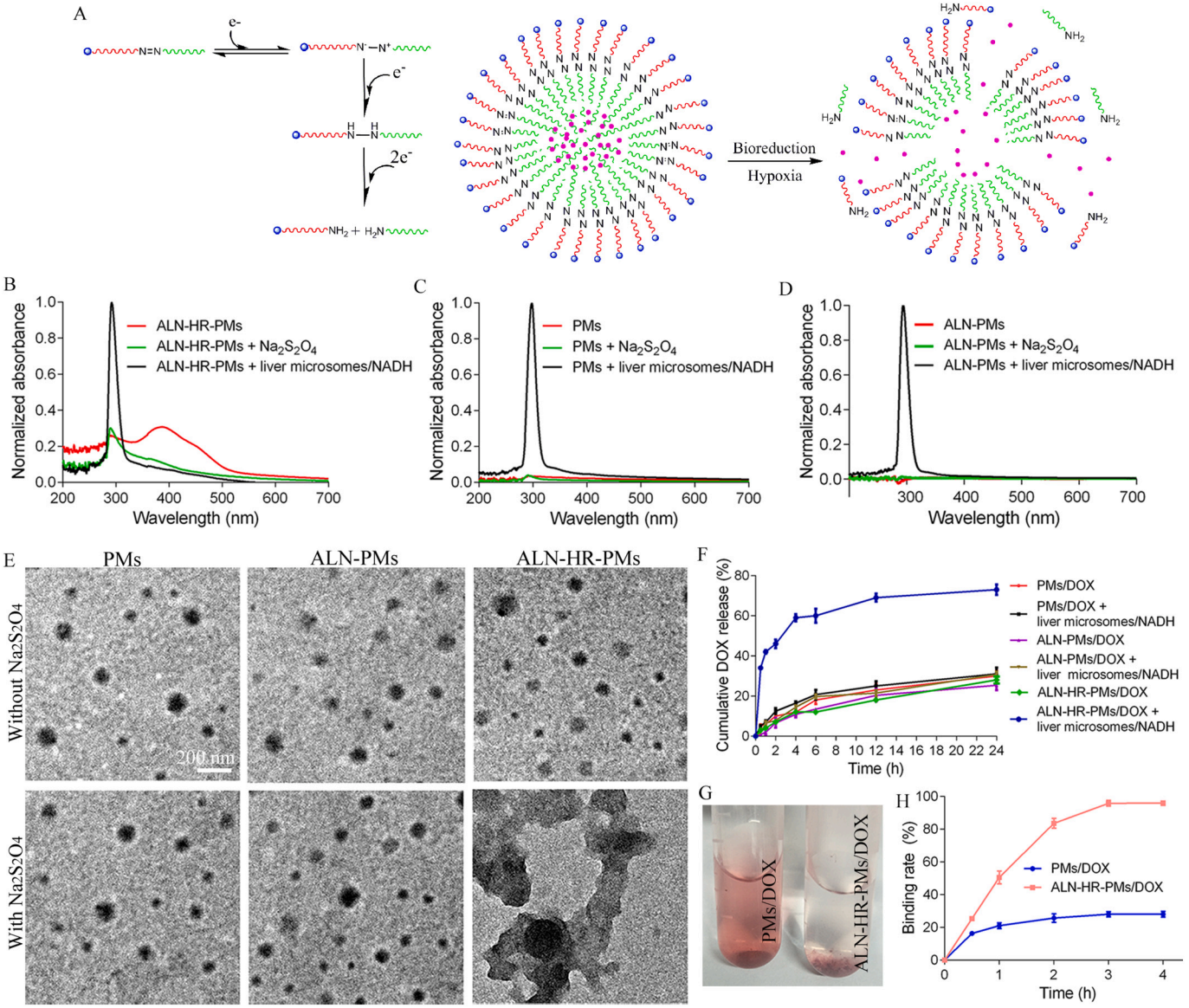

Fig. 2. *In vitro* response to hypoxia and bone-targeted efficiency evaluation. (A) schematic illustration of hypoxia-induced AZO cleavage for triggered drug release of ALN-HR-PMs. UV–vis spectra of (B) ALN-HR-PMs, (C) PMs, and (D) ALN-PMs before and after hypoxic treatment. (E) TEM images of PMs, ALN-PMs, and ALN-HR-PMs before and after hypoxic treatment. (F) Cumulative drug release of PMs, ALN-PMs, and ALN-HR-PMs before and after hypoxic treatment. (G) Optical photographs of binding of PMs and ALN-HR-PMs with water-insoluble HA and (H) corresponding binding rate. $Na_2S_2O_4$ and rat liver microsomes/NADH were used to generate the chemical and biological hypoxic conditions, respectively. Data were presented as mean ± SD ($n = 3$).

fluorescence intensity of DOX gradually increased from the normoxic edge to the hypoxic center in ALN-HR-PMs/DOX treated cells, as a result of hypoxia-induced disassembly of ALN-HR-PMs/DOX. No fluorescence difference between the edge and center was observed in AZO-free PMs/DOX or ALN-PMs/DOX treated cells (Fig. 3A). CLSM observation was further confirmed by line scanning. As revealed in Fig. 3B, the fluorescence intensity of DOX in AZO-free groups, acquired by Image J software, remained low (< 50) throughout the whole coverslip; comparatively, DOX intensity in ALN-HR-PMs/DOX treated cells was hypoxia-dependent, reaching its peak (> 200) in the mostly severe hypoxic center.

In the following, a hypoxia incubator was employed to study hypoxia-responsive drug release at the fixed oxygen conditions. In line with the results from the coverslip experiments, AZO-free PMs/DOX or ALN-PMs/DOX treated cells showed no difference in DOX intensity under normoxic (21% O_2) and hypoxic (1% O_2) conditions, while there was a stronger fluorescence for ALN-HR-PMs/DOX treated cells under hypoxic condition than under normoxic condition (Fig. 3C). Microscopic observation also revealed that the released DOX was mainly located in the cytoplasm without permeating into the nucleus. Hypoxia-responsive drug release was further quantitatively analyzed by flow cytometry (Fig. 3D). As expected, DOX release in AZO-free groups was similar under normoxic and hypoxic conditions (3.16/3.20 for PMs/DOX and 3.81/3.78 for ALN-PMs/DOX, hypoxia/normoxia); DOX release in ALN-HR-PMs/DOX treated cells was considerably accelerated under hypoxic condition, showing 2.02-fold higher than under normoxic condition (8.33/4.12). DOX intensity under normoxic condition could be also used to compare the difference in cell uptake of the micelles. It could be seen that cell uptake of PMs/DOX, ALN-PMs/DOX, and ALN-HR-PMs/DOX was 3.20, 3.78, and 4.12, respectively. The relatively high uptake of ALN-PMs/DOX in comparison to PMs/DOX should be due to ALN conjugation. This inference did not mean the existence of HA on the surface of RM-1 cells. The abundant hydroxyl groups should account for increased cell uptake through the formation of covalent bonds with

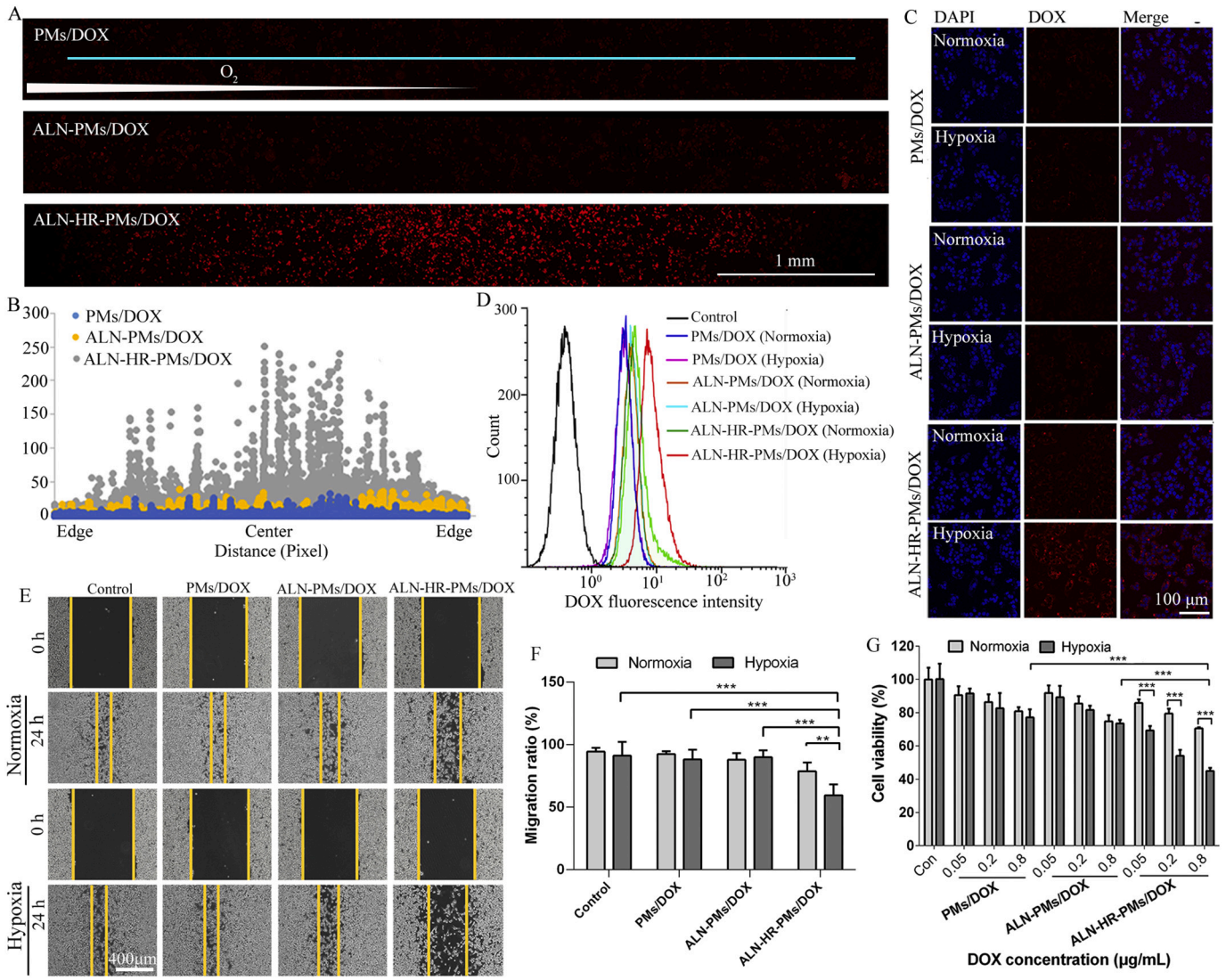

Fig. 3. Hypoxia-responsive intracellular drug release for improved anti-cancer *in vitro*. (A) CLSM observation of DOX release in RM-1 cells treated with PMs/DOX, ALN-PMs/DOX, and ALN-HR-PMs/DOX in a non-quantitative gradient hypoxia and (B) corresponding quantitative analysis by the line scanning. The cells were covered by a coverslip after removing drug-containing medium and the oxygen concentration decreased from the edge to center of the coverslip. (C) CLSM observation of DOX release in RM-1 cells treated with PMs/DOX, ALN-PMs/DOX, and ALN-HR-PMs/DOX under the fixed normoxic (21% O_2) and hypoxic (1% O_2) conditions generated by the hypoxia incubator. The nuclei were stained with DAPI. (D) Quantitative analysis of DOX fluorescence in RM-1 cells treated with PMs/DOX, ALN-PMs/DOX, and ALN-HR-PMs/DOX under normoxic and hypoxic conditions by flow cytometry. (E) Wound healing assay of RM-1 cells treated with PMs/DOX, ALN-PMs/DOX, and ALN-HR-PMs/DOX under normoxic and hypoxic conditions and (F) corresponding quantitative analysis. Data were acquired by Image J and expressed as mean ± SD ($n = 5$). $^{**}p < 0.01$ and $^{***}p < 0.001$. (G) MTT assay of PMs/DOX, ALN-PMs/DOX, and ALN-HR-PMs/DOX against RM-1 cells under normoxic and hypoxic conditions after 24 h incubation. Data were expressed as mean ± SD ($n = 6$). $^{***}p < 0.001$.

proteins on cell surface [25,39,40]. On the other hand, the higher uptake of ALN-HR-PMs/DOX might result from DOX release triggered by local hypoxia generated by clustered cell growth [41]. This result was in good consistence with the line scanning profiles, where ALN-HR-PMs/DOX generally showed high fluorescence intensity throughout the whole coverslip, even in the normoxic edge (Fig. 3B).

In vitro anti-cancer efficacy of the micelles under normoxic and hypoxic conditions was evaluated by wound healing assay and MTT assay against RM-1 cells. Wound healing assay showed that cell migration was effectively inhibited after treated with ALN-HR-PMs/DOX under hypoxic condition ($p < 0.01$, hypoxia *versus* normoxia), showing a significantly high inhibition ratio compared with the other groups ($p < 0.001$, ALN-HR-PMs/DOX *versus* PMs/DOX and ALN-PMs/DOX under hypoxic condition) (Fig. 3E and F). There was no difference observed in the cells treated with PMs/DOX, ALN-PMs/DOX, and ALN-HR-PMs/DOX under normoxic condition as well as in the cells treated with AZO-free PMs/DOX and ALN-PMs/DOX under normoxic and hypoxic conditions. MTT assay further confirmed that ALN-HR-PMs/DOX were of high cytotoxicity under hypoxic condition. As shown in Fig. 3F, three drug formulations exhibited DOX concentration-dependent cytotoxicity and AZO-free PMs/DOX and ALN-PMs/DOX had no difference under normoxic and hypoxic conditions; comparatively, the cytotoxicity of ALN-HR-PMs/DOX was considerably augmented under hypoxic condition, showing a significant difference compared with the other groups ($p < 0.001$, hypoxia *versus* normoxia; $p < 0.001$, ALN-HR-PMs/DOX *versus* PMs/DOX and ALN-PMs/DOX under hypoxic condition). MTT assay performed in MDA-MB-231 cells displayed a similar tread (supplementary Fig. S6). The results from wound healing assay and MTT assay were well consistent. Improved *in vitro* anti-cancer efficacy of ALN-HR-PMs/DOX under hypoxic condition indicates that internalized micelles remain a whole under normoxic condition for reduced side effect and however, intracellularly release DOX to a high therapeutic dosage under

hypoxic condition for improved bioavailability. ALN-HR-PMs/DOX can deliver DOX to cells *via* fusing with cell membrane, micropinocytosis after destabilization by cell membrane components when adsorbed on cell surface, or nanoparticle-mediated endocytosis [42]. Only nanoparticle-mediated endocytosis can ensure that the micelles are internalized as a whole. Thus, nanoparticle-mediated endocytosis is the key entry pathway for the micelles [43].

Additionally, the disassembly of ALN-HR-PMs composed of ALN-PEG-AZO-PLL copolymer under hypoxic condition will produce aniline, which is also toxic to cells and organs. Thereby, clarifying that

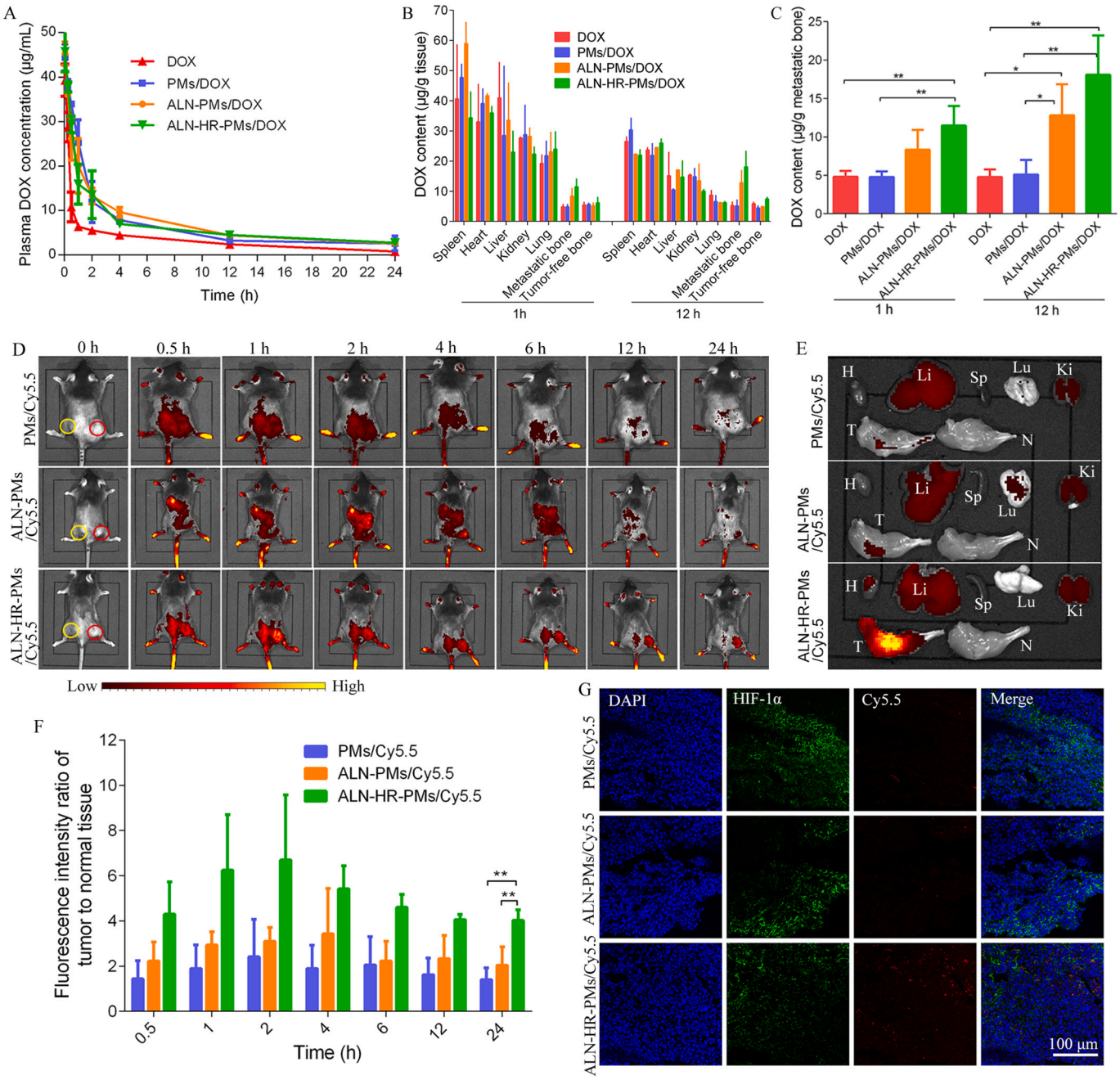

Fig. 4. Improved pharmacokinetic performance for bone-targeted drug delivery and subsequent hypoxia-responsive drug release. (A) The plasma DOX concentration over time. Healthy mice were intravenously injected with DOX, PMs/DOX, ALN-PMs/DOX, and ALN-HR-PMs/DOX at 5 mg DOX/kg body weight. (B and C) DOX content in spleen, heart, liver, kidney, lung, metastatic bone, and tumor-free bone at 1 h and 12 h post-injection. Tumor-bearing mice were intravenously injected with DOX, PMs/DOX, ALN-PMs/DOX, and ALN-HR-PMs/DOX at 5 mg DOX/kg body weight. Data were presented as mean ± SD ($n = 3$). *$p < 0.05$ and **$p < 0.01$. (D) *In vivo* NIR fluorescence images acquired at 0, 0.5, 1, 2, 4, 6, 12, and 24 h post-injection. Yellow circle indicated the tumor-free bone site and blue circle indicated the metastatic bone site. The color bar indicated fluorescence intensity from (red) low to high (yellow). (E) *Ex-vivo* fluorescence images of the tissues harvested from the mice after the last whole-body imaging. H: heart; Li: liver; Sp: spleen; Lu: lung; Ki: kidney; T: tumor-bearing metastatic bone; N: normal contralateral tumor-free bone. (F) Fluorescence ratio of the metastatic bone site to the tumor-free bone site. The fluorescence intensity of the selected sites indicated by yellow or blue circle was acquired by IVIS imaging software. Data were presented as mean ± SD (n = 3). **$p < 0.01$. (G) *In vivo* immunofluorescence staining of the tumor tissue stripped from the metastatic bone after *ex-vivo* fluorescence imaging. For NIR imaging and immunofluorescence staining, tumor-bearing mice were intravenously injected with 100 μL of PMs/Cy5.5, ALN-PMs/Cy5.5, and ALN-HR-PMs/Cy5.5. (For interpretation of the references to color in this figure legend, the reader is referred to the web version of this article.)

hypoxia-responsive drug release of ALN-HR-PMs but not the production of aniline contributes to increased cytotoxicity is necessary. As revealed in supplementary Fig. S7A, blank ALN-HR-PMs with the concentrations ranging from 1 to 100 μg/mL exhibited a slight cytotoxicity comparable to that of PMs and ALN-PMs under normoxic and hypoxic conditions. This slight cytotoxicity should originate from highly positive surface of the micelles since positively charged nanoparticle always have a relatively high cytotoxicity in contrast to negatively charged and neutral ones [44]. Importantly, based on drug loading capacity shown in supplementary Table S1 and MTT assay shown in Fig. 3G, the concentration of blank ALN-HR-PMs was far less than 100 μg/mL at the used DOX concentrations and thus, the cytotoxicity of blank ALN-HR-PMs under hypoxic condition was ignorable. Blank ALN-HR-PMs also exhibited ignorable cytotoxicity against MDA-MB-231 cells (supplementary Fig. S7B). Taken together, the above results suggested that ALN-HR-PMs were biocompatible and showed improved anti-cancer efficacy under hypoxic condition, as a result of hypoxia-responsive drug release.

3.3. Pharmacokinetics, tissue distribution, and hypoxia-responsive drug release in vivo

There is substantial evidence showing that encapsulating a drug into nanocarriers with PEGylated surface can considerably improve its pharmacokinetic profile through their protective effect against degradation, protein adsorption, and subsequent systemic clearance [45]. PMs/DOX should be of improved pharmacokinetic profile compared with DOX and however, determining whether their pharmacokinetic profile will be impaired after ALN conjugation and AZO insertion is still necessary. To this end, the mice received intravenous injection of DOX, PMs/DOX, ALN-PMs/DOX, and ALN-HR-PMs/DOX at equivalent DOX dosage and the time-dependent plasma drug concentration was determined by HPLC. As shown in Fig. 4A, the plasma drug concentration of all drug formulations peaked very quickly following injection and almost bottomed out at 24 h post-injection. Nevertheless, the concentration of PMs/DOX, ALN-PMs/DOX, and ALN-HR-PMs/DOX generally decreased more slowly than DOX. To better compare pharmacokinetic profile, the plasma drug concentration-time curves were then fitted into a two-compartment model using PK Solver software and the main pharmacokinetic parameters such as the distribution half-life ($t_{1/2\alpha}$), elimination half-life ($t_{1/2\beta}$), the area under the curve ($AUC_{0\rightarrow\infty}$), clearance rate (CL), elimination rate constant (K_{10}), and mean residence time (MRT) of the drug formulations were obtained (Table 1). It could be seen that the pharmacokinetic parameters of DOX were improved after encapsulated; PMs/DOX, ALN-PMs/DOX, and ALN-HR-PMs/DOX were distributed and eliminated more slowly than DOX with significant difference in $t_{1/2\alpha}$, $t_{1/2\beta}$, $AUC_{0\rightarrow\infty}$, CL, and K_{10}, indicating their prolonged blood circulation time. Moreover, there was no significant difference observed among DOX-loaded micelles, indicating ALN conjugation and AZO insertion had no significant role in the pharmacokinetic profile of the micelles.

There are several *in vitro* and *in vivo* bone metastasis models. Injecting tumor cells such as breast, prostate, or multiple myeloma, into unilateral femur of mice is the most common for preclinical study, which is also a classic model to evaluate cancer-induced bone pain [46]. Herein, bone metastasis model was established by injecting RM-1 cells into the femur of the right limb of mice. In the following, tumor-bearing mice received injection of different drug formulations and DOX content in some important tissues including spleen, heart, liver, kidney, lung, metastatic bone, and contralateral tumor-free bone at 1 h and 12 h post-injection was measured to evaluate drug tissue distribution. As shown in Fig. 4B, all drug formulations were widely distributed in all tissues and the drug distribution in spleen, heart, liver, kidney, and lung was relatively high at 1 h post-injection, due to non-specific uptake by macrophages in the reticuloendothelial system (RES) of normal tissues, which subsequently decreased over time. DOX content of ALN-free DOX and PMs/DOX remained at a relatively low level in the tumor-free and metastatic bones, indicating the difficulty in delivering therapeutic agents to bone without a targeting effect. Increasingly accumulated DOX content in the metastatic bone was only observed in ALN-PMs/DOX and ALN-HR-PMs/DOX groups, showing a significant difference compared with DOX and PMs/DOX ($p < 0.01$, ALN-HR-PMs/DOX *versus* DOX and PMs/DOX at 1 h and 12 h post-injection; $p < 0.05$, ALN-PMs/DOX *versus* DOX and PMs/DOX at 12 h post-injection). Metastatic bone is of corrosive bone surface consisting of highly crystalline HA, while healthy bone is mainly composed of amorphous HA [17]. ALN is more easily combined with highly crystalline HA, resulting in a higher accumulation of ALN-PMs/DOX and ALN-HR-PMs/DOX in the metastatic bone than in the tumor-free bone. Moreover, although there was no significant difference found, ALN-HR-PMs/DOX showed a generally higher accumulation in the metastatic bone than ALN-PMs/DOX, which was due to hypoxia-responsive release of ALN-HR-PMs/DOX. DOX content in tissues determined by HPLC comprised released and unreleased DOX and in light of this, ALN-PMs/DOX and ALN-HR-PMs/DOX should be of approximate DOX content in the metastatic bone. This unexpected discrepancy might result from the fact that unreleased DOX was not detected totally by HPLC method, offering an explanation that the micelles did not show a relatively high drug distribution in the normal tissues in comparison to DOX, although the former had improved pharmacokinetic performance. This also offered an explanation that ALN-functionalized micelles did not have a higher drug accumulation in the normal tissues than ALN-free micelles, although ALN was easily internalized by macrophages [47]. Similar phenomena were also described by others [17,40,48].

In vivo NIR imaging was further carried out to substantiate bone-targeted drug delivery and subsequent hypoxia-responsive intratumoral drug release of ALN-HR-PMs. DOX is not suitable for *in vivo* imaging as its fluorescence in visible range is severely interfered by autofluorescence from biological tissues. Cy5.5 is thus loaded into the micelles, forming ALN-HR-PMs/Cy5.5 as well as PMs/Cy5.5 and ALN-PMs/Cy5.5 for the whole-body NIR imaging. As revealed in Fig. 4D, all Cy5.5-loaded micelles were quickly distributed throughout the body following injection. Although Cy5.5 accumulation in the metastatic bone, facilitated by the EPR effects, was found in all groups, the fluorescence in the metastatic bone in PMs/Cy5.5 group almost disappeared at 24 h post-injection, indicating that the EPR effects was not effective enough for drug delivery to bone using traditional nanocarriers. For ALN-PMs/Cy5.5 group, although bone-targeted delivery was achieved, as validated by their relatively strong fluorescence signal in the metastatic bone, accumulated Cy5.5 was shielded inside the micelles, resulting in the weak fluorescence signal. A stronger fluorescence signal in the metastatic bone was observed in ALN-HR-PMs/Cy5.5 group, as a result of hypoxia-responsive drug release following accumulation. *Ex vivo* tissue-specific imaging also confirmed the above results, where ALN-HR-PMs/Cy5.5 displayed the strongest fluorescence signal in the metastatic bone (Fig. 4E). No high Cy5.5 accumulation in the tumor-free bone was observed in all groups, also indicating that ALN had no strong affinity to healthy bone. These results were well consistent with drug tissue distribution results. NIR imaging result was then quantitatively

Table 1
Pharmacokinetic parameters of DOX after intravenous injection of DOX, PMs/DOX, ALN-PMs/DOX, and ALN-HR-PMs/DOX at 5 mg DOX/kg body weight ($n = 3$). $^{*}p < 0.05$, $^{**}p < 0.01$, and $^{***}p < 0.001$ *versus* DOX.

Parameters	$T_{1/2\alpha}$(h)	$T_{1/2\beta}$(h)	$AUC_{0\rightarrow\infty}$ (μg/mL·h)	CL (mL/g·h)	K_{10} (1/h)	MRT (h)
DOX	0.24	11.73	97.78	8.47	0.48	14.51
PMs/DOX	1.04***	19.08*	265.87***	3.14*	0.18***	21.21*
ALN-PMs/DOX	0.98**	21.40*	282.05***	3.07*	0.18***	25.36*
ALN-HR-PMs/DOX	0.77*	21.97*	232.14**	3.34*	0.23**	26.97*

analyzed by calculating the fluorescence ratio of metastatic bone site to tumor-free bone site. As shown in Fig. 4F, the ratio of ALN-HR-PMs/Cy5.5 was generally higher than that of AZO-free groups, showing a significant difference at 24 h post-injection ($p < 0.01$ *versus* PMs/Cy5.5 and ALN-PMs/Cy5.5), while no significant difference was found between PMs/Cy5.5 and ALN-PMs/Cy5.5. Moreover, in comparison to PMs/Cy5.5 and ALN-PMs/Cy5.5, ALN-HR-PMs/Cy5.5 showed a stronger fluorescence signal in the metastatic bone than in the normal tissues such as liver and kidney. It is reported that only a very small proportion of injected drugs even encapsulated in nanocarriers can be accumulated in tumor and most of them are non-specifically accumulated in some normal tissues, resulting from RES recognition. Therefore, the higher fluorescence signal in the metastatic bone than in the liver and kidney suggested that ALN-HR-PMs could retain their payload in normal tissues for reduced side effects, while specifically releasing it in the metastatic bone to achieve an effective therapeutic dosage.

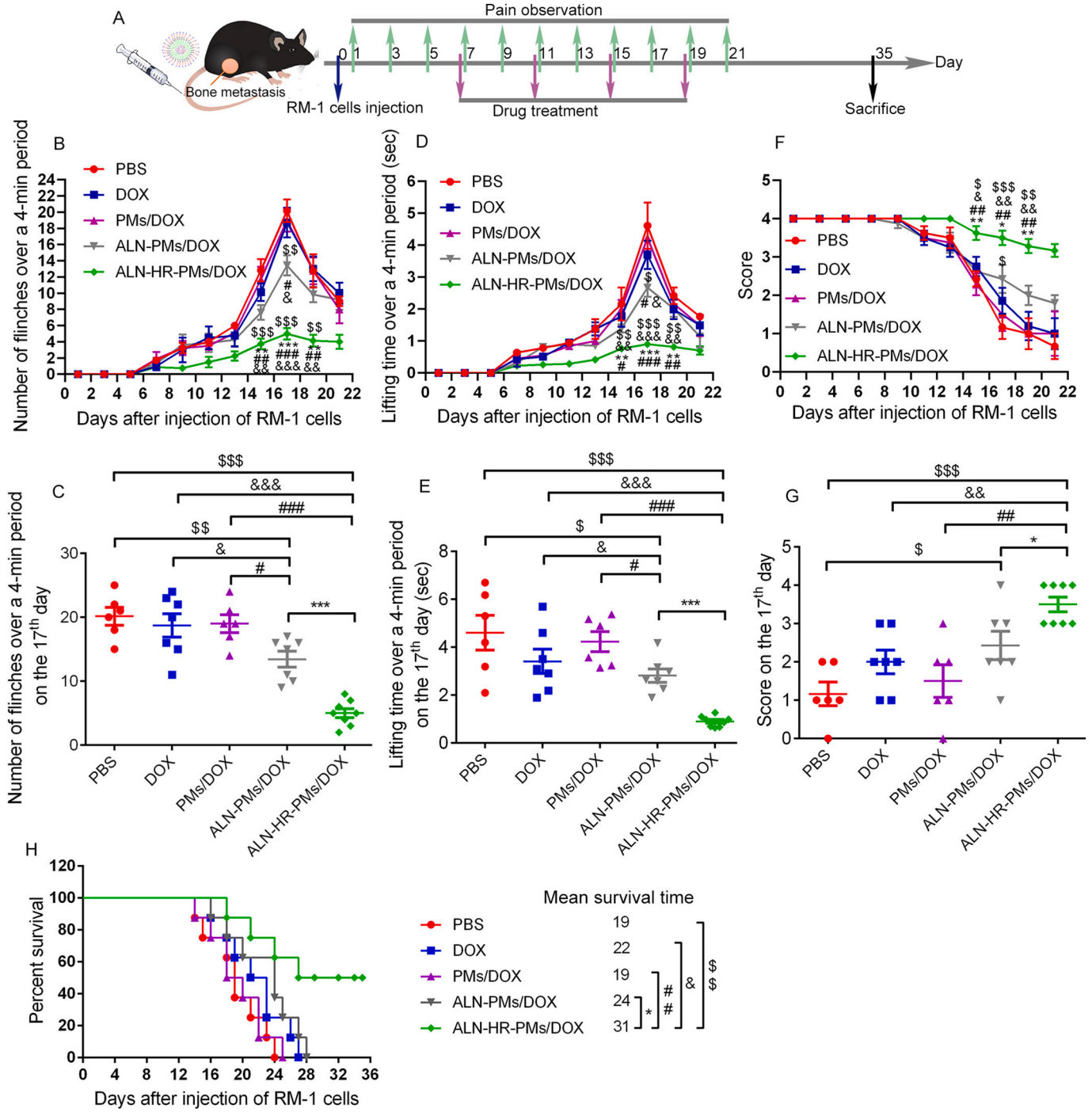

Fig. 5. *In vivo* anti-cancer efficacy. (A) Protocol of drug treatment for cancer-induced spontaneous pain evaluation. When cancer-induced pain was observed on the 7th day, the mice were intravenously injected with PBS, DOX, PMs/DOX, ALN-PMs/DOX, and ALN-HR-PMs/DOX at 5 mg DOX/kg body weight every four days. (B and C) Number of flinches, (D and E) lifting time, and (G and F) score for the use of tumor-bearing limb over a 4-min period. Four, three, two, one, and zero scores represented normal use, occasional limping, partial non-use, substantial non-use, and non-use of tumor-bearing limb, respectively. (H) Survival situation analysis of tumor-bearing mice. Data were presented as mean ± SD ($n = 8$); $^{*}p < 0.05$, $^{**}p < 0.01$, and $^{***}p < 0.001$ *versus* ALN-PMs/DOX; $^{\#}p < 0.05$, $^{\#\#}p < 0.01$, and $^{\#\#\#}p < 0.001$ *versus* PMs/DOX; $^{\&}p < 0.05$, $^{\&\&}p < 0.01$, and $^{\&\&\&}p < 0.001$ *versus* DOX; $^{\$}p < 0.05$, $^{\$\$}p < 0.01$, and $^{\$\$\$}p < 0.001$ *versus* PBS.

After *Ex vivo* tissue-specific imaging, the tumor tissue was stripped from the metastatic bone for immunofluorescence staining. HIF-1α (hypoxia inducible factor 1α), oxygen-labile α subunit of HIFs, is a key regulator of cellular responses to hypoxia and its overexpression is highly correlated with hypoxia. Immunofluorescence staining revealed that HIF-1α was over-expressed in all bone metastatic tumor tissues and in the HIF-1α overexpression region, a weak Cy5.5 fluorescence was observed in PMs/Cy5.5 and ALN-PMs/Cy5.5 groups, while a relatively strong fluorescence was observed in ALN-HR-PMs/Cy5.5 group (Fig. 4G). The immunofluorescence staining result fitted with NIR imaging result well, which was also a validation that ALN-HR-PMs could sensitively respond to hypoxic bone metastasis.

3.4. *In vivo anti-cancer efficacy*

Most literature evaluating bone-targeted drug carriers for bone metastasis focus on tumor inhibition efficacy while neglecting the other important clinical aspects. Cancer-induced bone pain is the most prevalent symptom of patients with bone metastasis. Bone pain relief is particularly important for improving patients' quality of life and also emerges as an index of anti-cancer efficacy. To evaluate *in vivo* anti-cancer efficacy, tumor-bearing mice began to receive drug treatment every four days when cancer-induced spontaneous bone pain, such as number of flinches and lifting time, was observed (Fig. 5A). As shown in Fig. 5B and C, the mice quickly recovered from the surgery for bone metastasis model establishment, showing no problem in walking on the 1st, 3rd, and 5th days. Slight pain with a small number of flinches over a 4-min period was observed on the 7th day in all groups. The number of flinches in PBS, DOX and PMs/DOX groups quickly increased over time, reaching peak on the 17th day, and subsequently decreased, probably due to aggravated tumor burden. Compared with PBS, DOX, and PMs/DOX groups, ALN-PMs/DOX group showed slightly reduced number of flinches with considerable difference on the 17th day ($p < 0.05$ *versus* DOX and PMs/DOX; $p < 0.01$ *versus* PBS), but not at any other time points. Remarkably reduced number of flinches was observed in ALN-HR-PMs/DOX group on the 15th, 17th, and 19th days. For example, on the 17th day, ALN-HR-PMs/DOX group was significantly different from PBS, DOX, PMs/DOX, and ALN-PMs/DOX groups ($p < 0.001$). Moreover, the number of flinches in ALN-HR-PMs/DOX group generally remained at a relatively low level. Spontaneous lifting time exhibited nearly the same tread as number of flinches and similarly, ALN-HR-PMs/DOX group showed significantly short lifting time in comparison to PBS, DOX, PMs/DOX, and ALN-PMs/DOX groups (Fig. 5D and E). The level of pain was further scored by the use of tumor-bearing limb. As depicted in Fig. 5F and G, the limb use in ALN-HR-PMs/DOX group appeared normal with occasional limping, showing a significant difference compared with the other groups, especially on the 15th, 17th, and 19th days. Taken together, PBS, DOX, and PMs/DOX groups exhibited almost the same pain behaviors without any significant differences among them throughout the experiment, corroborating the fact that traditional chemotherapy and nanomedicine were not effective in treating bone metastasis. Although a bone-targeted effect was achieved for ALN-PMs/DOX, as validated by drug tissue distribution data, their efficacy in relieving pain was unsatisfactory. ALN-HR-PMs/DOX could significantly relieve pain, as a result of bone-targeted accumulation followed by hypoxia-responsive release to achieve an effective therapeutic dosage in the metastatic bone. Additionally, it was worth pointing out that ALN in ALN-PMs/DOX and ALN-HR-PMs/DOX acted as a bone-targeted moiety more than as an anti-resorptive agent for pain relief. Bioavailability loss when its amino group was used for conjugation with copolymer and/or insufficient dosage might contribute to its restricted therapeutic outcome. On the other hand, as mentioned above, its binding with bone relied on hydroxyl and phosphonate groups, and thus its bone-targeted ability was not affected.

Pain behaviors of the mice reflected their survival situation well. As demonstrated in Fig. 5F, the mean survival times of PBS, DOX, PMs/DOX, ALN-PMs/DOX, and ALN-HR-PMs/DOX groups were 19, 22, 19, 24, and 31 days, respectively. ALN-HR-PMs/DOX significantly prolonged survival time of the mice ($p < 0.05$ *versus* DOX and ALN-PMs/DOX; $p < 0.01$ *versus* PBS and PMs/DOX). Notably, non-targeted PMs/DOX even promoted death compared with DOX. Although the accumulation of PMs/DOX in metastatic bone was at least not less than that of DOX, according to tissue distribution data, their slow and sustained drug release behavior might make local therapeutic dosage even lower than free DOX. This result also indicated that for nanocarriers, effective drug accumulation in metastatic bone followed by rapid drug release to an effective therapeutic dosage was very crucial for treating bone metastasis.

In another experiment, tumor-bearing mice were treated (Fig. 6A) and metastatic bones from tumor-bearing mice as well as healthy bone from healthy mice were harvested on the 21st day for Micro-CT and histopathological analysis. Digital photos revealed that the metastatic bone in PBS group was heavily burdened with tumor and tumor cells had expanded out of bone, forming a solid tumor around bone. After treated with DOX, PMs/DOX, and ALN-PMs/DOX, tumor burden was reduced in some extent. Encouragingly, the metastatic bone in ALN-HR-PMs/DOX group appeared to be same with the healthy bone in shape (Fig. 6B). Micro-CT scanning provided more information about the metastatic bones. Micro-CT 2D images demonstrated that compared with the healthy bone, bone morphology and structure of metastatic bones was severely damaged, showing severe facture in PBS group. DOX and PMs/DOX seemed to have no beneficial effect on protecting metastatic bone against fracturing, although reduced tumor burden was observed in these two groups; bone loss could still be seen in ALN-PMs/DOX group. Desirable therapeutic outcome was observed in ALN-HR-PMs/DOX group, showing no fracture (Fig. 6C). The 3D reconstruction further indicated the surface of the healthy bone was smooth and flat, while it became incomplete and rough, once metastasized. Especially, 3D imaging results demonstrated that compared with the other groups, ALN-HR-PMs/DOX could effectively inhibit bone destruction, maintaining its shape and integrity well, although bone surface of this group was still a little rough, due to tumor erosion (Fig. 6D). Bone metrics such as BMD and Tb.N were also evaluated (Fig. 6E and F). Bone metrics in ALN-HR-PMs/DOX group were significantly better than those in PBS, DOX, PMs/DOX, and ALN-PMs/DOX groups, which were comparable to those in the healthy bone. No significant difference was found among DOX, PMs/DOX, and ALN-PMs/DOX groups and between healthy and ALN-HR-PMs/DOX groups.

After stripping tumor tissue, the harvested bones were decalcified for H&E, TRAP, ALP, and TRAP/ALP staining (Fig. 6G). H&E staining showed that almost all cells in bone marrow were necrotic in PBS group. Although alive cells in bone marrow increased, a lot of necrotic cells were still observed in DOX, PMs/DOX, and ALN-PMs/DOX groups. Noting that the region with many necrotic cells in bone marrow was also denoted as tumor in the literature [49]. As expected, the metastatic bone in ALN-HR-PMs/DOX group was histologically similar to the healthy bone, indicating that tumor growth was dramatically inhibited. There is a dynamic balance between osteoclast-mediated bone resorption and osteoblast-mediated bone formation for bone turnover in healthy bone [50]. TRAP and ALP are two biomarkers used to detect osteoclast and osteoblast activities in bone, respectively. TRAP, ALP, and TRAP/ALP staining revealed that osteoclasts stained as wine red and osteoblasts stained as dark brown were mostly concentrated on bone/bone marrow interface and around trabecular bone [51], respectively. Bone turnover was imbalanced and osteoclast activity increased, while osteoblast activity decreased in PBS, DOX, PMs/DOX, and ALN-PMs/DOX groups. It indicated that bone resorption was predominant over bone formation in these groups, thus leading to bone destruction, as revealed in Micro-CT imaging (Fig. 6C and D). Moreover, although bone metastatic prostate cancer is reported to be preponderantly osteoblastic [52], it is osteolytic in this work, inferring that bone metastasis phenotype is mainly determined by tumor cell type. After ALN-HR-PMs/DOX treatment, bone

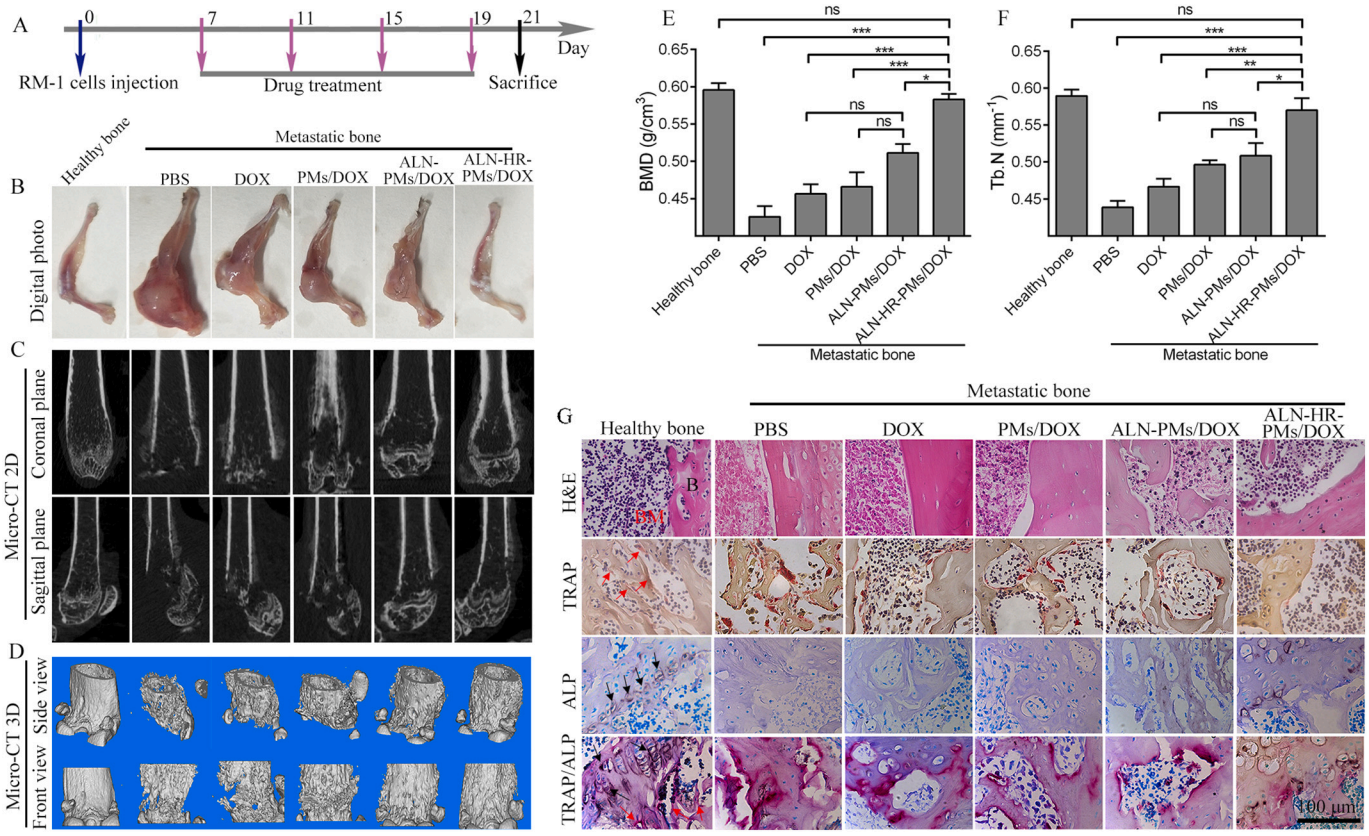

Fig. 6. Bone histological evaluation. (A) Protocol of drug treatment for histological evaluation. On the 7th day after RM-1 cells injection, the mice were intravenously injected with PBS, DOX, PMs/DOX, ALN-PMs/DOX, and ALN-HR-PMs/DOX at 5 mg DOX/kg body weight every four days, and metastatic bones as well as healthy bone were harvested for histological evaluation on the 21st day. The bone from healthy mice without bearing tumor and drug treatment was denoted as healthy bone and was also evaluated for comparison. (B) Digital photos, (C) Micro-2D imaging, and (D) Micro-CT 3D reconstruction of metastatic bones as well as healthy bone. (E) BMD and (F) Tb.N parameters of metastatic bones as well as healthy bone acquired from (D). Data were presented as mean ± SD ($n = 3$); $^{*}p < 0.05$, $^{**}p < 0.01$, and $^{***}p < 0.001$. (G) H&E, TRAP, ALP, and TRAP/ALP staining of metastatic bones as well as healthy bone. B: bone; BM: bone marrow. Black arrows indicated osteoclasts stained as wine red and red arrows indicated osteoblasts stained as dark brown. (For interpretation of the references to color in this figure legend, the reader is referred to the web version of this article.)

turnover balance was re-established, showing decreased osteoclast activity and increased osteoblast activity, and resultant bone microenvironment was similar to the healthy bone. Quantitative analysis further demonstrated that osteoclast activity in ALN-HR-PMs/DOX group was significantly low, while osteoblast activity was significantly high, compared with DOX, PMs/DOX, and ALN-PMs/DOX groups (Supplementary Fig. S8). Together, histological examination corroborated that ALN-HR-PMs/DOX were able to inhibit tumor growth and thus balance bone turnover by inhibiting osteoclast activity and promoting osteoblast activity for relieved bone pain and prolonged survival time.

Previously reported ALN-functionalized nanocarriers aim to improve therapeutic outcome by increasing drug accumulation in metastatic bone through bone-targeted effect of ALN. We develop ALN-functionalized hypoxia-responsive nanocarriers, aiming to improve therapeutic outcome by maximize drug bioavailability *via* hypoxia-responsive drug release after bone-targeted effect is achieved. The results demonstrate that therapeutic outcome of ALN-functionalized nanocarriers is significantly augmented, once endowed with hypoxia-responsive feature, showing the outstanding advantage over conventional ALN-functionalized nanocarriers. Additionally, it is worth noting that ALN-functionalized nanocarriers always exhibit significantly improved therapeutic outcome in comparison to non-functionalized nanocarriers in the literature, while no significant difference between them is observed in this work, displaying one of advantages of designed ALN-functionalized copolymer. Conjugating ALN with abundant amino groups of PLL to increase ALN content in the copolymers for synergistic effect of ALN and loaded DOX is an alternative to solve this issue.

Contralateral tumor-free bones of tumor-bearing mice were also harvested for histological evaluation by H&E, TRAP, ALP, and TRAP/ALP staining. As shown in supplementary Fig. S9, tumor-free bones in all drug-treated groups were histologically similar to the healthy bone from tumor-free mice. ALN-HR-PMs/DOX were therefore safe to healthy bone, benefiting from their affinity to metastatic bone. Moreover, some important tissues including heart, liver, spleen, lung, and kidney were also harvested for H&E staining (Supplementary Fig. S10). The results showed that free DOX was toxic to heart, which was mainly characterized by myocardial disruption. No considerable toxicity to heart was observed in the other groups and no considerable toxicity to liver, spleen, lung, and kidney was observed in all groups. ALN-HR-PMs/DOX were therefore a biocompatible drug delivery system.

4. Conclusion

In summary, we prepared alendronate-functionalized hypoxia-responsive polymeric micelles as drug carrier for effective treatment of bone metastatic prostate cancer. *In vitro* studies revealed that the prepared micelles were highly sensitive to hypoxia and were more toxic to hypoxic tumor cells. *In vivo* studies showed that after a targeted accumulation in metastatic bone, the micelles could rapidly release their payload to an effective therapeutic dosage in responding to hypoxic bone metastasis microenvironment. As a result, the micelles could effectively suppress tumor growth and preserve bone structure by

inhibiting osteoclast activity and promoting osteoblast activity, achieving an enhanced therapeutic outcome with relieved bone pain and prolonged survival time. The micelles therefore emerged as a reliable drug delivery system for treating bone metastasis.

Declaration of Competing Interest

The authors declare no competing financial interests.

Acknowledgments

The work was supported by the National Natural Science Foundation of China (81401506, 81971131, and 81873924) and the Open Research Fund of State Key Laboratory of Bioelectronics, Southeast University (OPSKLB202007).

Appendix A. Supplementary data

Supplementary data to this article can be found online at https://doi.org/10.1016/j.jconrel.2021.04.035.

References

[1] M.E. Sowder, R.W. Johnson, Bone as a preferential site for metastasis, JBMR Plus 3 (2019), e10126.
[2] S. D'Oronzo, R. Coleman, J. Brown, F. Silvestris, Metastatic bone disease: pathogenesis and therapeutic options up-date on bone metastasis management, J. Bone Oncol. 15 (2019) 100205.
[3] G.D. Roodman, T.A. Guise, Chapter 22 - bone and cancer, in: D.B. Burr, M.R. Allen (Eds.), Basic and Applied Bone Biology, Second edition, Academic Press, 2019, pp. 411–423.
[4] C. Kan, G. Vargas, F. Le Pape, P. Clezardin, Cancer cell colonisation in the bone microenvironment, Int. J. Mol. Sci. 17 (2016) 1–16.
[5] I.M. Adjei, M.N. Temples, S.B. Brown, B. Sharma, Targeted nanomedicine to treat bone metastasis, Pharmaceutics 10 (2018) 205.
[6] C. Shi, T.T. Wu, Y. He, Y. Zhang, D.H. Fu, Recent advances in bone-targeted therapy, Pharmacol. Ther. 207 (2020) 107473.
[7] H.H. Van Acker, S. Anguille, Y. Willemen, E.L. Smits, V.F. Van Tendeloo, Bisphosphonates for cancer treatment: mechanisms of action and lessons from clinical trials, Pharmacol. Ther. 158 (2016) 24–40.
[8] B.A. Gartrell, F. Saad, Managing bone metastases and reducing skeletal related events in prostate cancer, Nat. Rev. Clin. Oncol. 11 (2014) 335–345.
[9] L.M.S. Boevé, M.C.C.M. Hulshof, A.N. Vis, A.H. Zwinderman, J.W.R. Twisk, W.P. J. Witjes, K.P.J. Delaere, R.J.A.V. Moorselaar, P.C.M.S. Verhagen, G. Van Andel, Effect on survival of androgen deprivation therapy alone compared to androgen deprivation therapy combined with concurrent radiation therapy to the prostate in patients with primary bone metastatic prostate cancer in a prospective randomised Clinical Trial: Data from the HORRAD Trial, Eur. Urol. 75 (2019) 410–418.
[10] E. Akoury, P. Ahangar, A. Nour, J. Lapointe, K.-P. Guérard, L. Haglund, D. H. Rosenzweig, M.H. Weber, Low-dose zoledronate for the treatment of bone metastasis secondary to prostate cancer, Cancer Cell Int. 19 (2019) 28.
[11] H. Cheng, A. Chawla, Y. Yang, Y. Li, J. Zhang, H.L. Jang, A. Khademhosseini, Development of nanomaterials for bone-targeted drug delivery, Drug Discov. Today 22 (2017) 1336–1350.
[12] C.F. Mu, J.L. Shen, J. Liang, H.S. Zheng, Y. Xiong, Y.H. Wei, F.Z. Li, Targeted drug delivery for tumor therapy inside the bone marrow, Biomaterials 155 (2018) 191–202.
[13] H. Cheng, A. Chewla, Y.F. Yang, Y.X. Li, J. Zhang, H.L. Jang, A. Khademhosseini, Development of nanomaterials for bone-targeted drug delivery, Drug Discov. Today 22 (2017) 1336–1350.
[14] X.Z. Ke, W. Lin, X.K. Li, H.L. Wang, X. Xiao, Z. Guo, Synergistic dual-modified liposome improves targeting and therapeutic efficacy of bone metastasis from breast cancer, Drug Deliv. 24 (2017) 1680–1689.
[15] T.T. Pham, H.T. Nguyen, C.D. Phung, S. Pathak, S. Regmi, D.-H. Ha, J.O. Kim, C. S. Yong, S.K. Kim, J.-E. Choi, S. Yook, J.-B. Park, J.-H. Jeong, Targeted delivery of doxorubicin for the treatment of bone metastasis from breast cancer using alendronate-functionalized graphene oxide nanosheets, J. Ind. Eng. Chem. 76 (2019) 310–317.
[16] S.B. Bai, D.Z. Liu, Y. Cheng, H. Cui, M. Liu, M.X. Cui, B.L. Zhang, Q.B. Mei, S. Y. Zhou, Osteoclasts and tumor cells dual targeting nanoparticle to treat bone metastases of lung cancer, Nanomed-Nanotechnol. 21 (2019) 102054.
[17] Y. Wang, Q. Huang, X. He, H. Chen, Y. Zou, Y. Li, K. Lin, X. Cai, J. Xiao, Q. Zhang, Y. Cheng, Multifunctional melanin-like nanoparticles for bone-targeted chemo-photothermal therapy of malignant bone tumors and osteolysis, Biomaterials 183 (2018) 10–19.
[18] P. Lavrador, V.M. Gaspar, J.F. Mano, Stimuli-responsive nanocarriers for delivery of bone therapeutics - barriers and progresses, J. Control. Release 273 (2018) 51–67.
[19] W.J. Zhang, I. Bado, H. Wang, H.C. Lo, X.H.F. Zhang, Bone metastasis: find your niche and fit in, Trends Cancer 5 (2019) 95–110.
[20] R. Kumari, D. Sunil, R.S. Ningthoujam, Hypoxia-responsive nanoparticle based drug delivery systems in cancer therapy: an up-to-date review, J. Control. Release 319 (2020) 135–156.
[21] Y. Li, J. Jeon, J.H. Park, Hypoxia-responsive nanoparticles for tumor-targeted drug delivery, Cancer Lett. 490 (2020) 31–43.
[22] Y. Li, A.L. Lu, M.M. Long, L. Cui, Z.P. Chen, L. Zhu, Nitroimidazole derivative incorporated liposomes for hypoxia-triggered drug delivery and enhanced therapeutic efficacy in patient-derived tumor xenografts, Acta Biomater. 83 (2019) 334–348.
[23] M.M. Long, A.L. Lu, M. Lu, L.Y. Weng, Q.P. Chen, L. Zhu, Z.P. Chen, Azo-inserted responsive hybrid liposomes for hypoxia-specific drug delivery, Acta Biomater. 115 (2020) 343–357.
[24] M. Nagae, T. Hiraga, T. Yoneda, Acidic microenvironment created by osteoclasts causes bone pain associated with tumor colonization, J. Bone Miner. Metab. 25 (2007) 99–104.
[25] S. Feng, Z.X. Wu, Z. Zhao, J. Liu, K. Sun, C. Guo, H. Wang, Z. Wu, Engineering of bone- and CD44-dual-targeting redox-sensitive liposomes for the treatment of orthotopic osteosarcoma, ACS Appl. Mater. Interfaces 11 (2019) 7357–7368.
[26] R.W. Johnson, M.E. Sowder, A.J. Giaccia, Hypoxia and bone metastatic disease, Curr. Osteoporos. Rep. 15 (2017) 231–238.
[27] F.F. Wang, L. Chen, R. Zhang, Z.P. Chen, L. Zhu, RGD peptide conjugated liposomal drug delivery system for enhance therapeutic efficacy in treating bone metastasis from prostate cancer, J. Control. Release 196 (2014) 222–233.
[28] T. Thambi, S. Son, D.S. Lee, J.H. Park, Poly(ethylene glycol)-b-poly(lysine) copolymer bearing nitroaromatics for hypoxia-sensitive drug delivery, Acta Biomater. 29 (2016) 261–270.
[29] C. Lim, J. Moon, T. Sim, W.R. Won, E.S. Lee, Y.S. Youn, K.T. Oh, A nano-complex system to overcome antagonistic photo-chemo combination cancer therapy, J. Control. Release 295 (2019) 164–173.
[30] Z. Zhao, Y. Zhao, C. Xie, C. Chen, D. Lin, S. Wang, D. Lin, X. Cui, Z. Guo, J. Zhou, Dual-active targeting liposomes drug delivery system for bone metastatic breast cancer: synthesis and biological evaluation, Chem. Phys. Lipids 223 (2019) 104785.
[31] W. Piao, S. Tsuda, Y. Tanaka, S. Maeda, F.Y. Liu, S. Takahashi, Y. Kushida, T. Komatsu, T. Ueno, T. Terai, T. Nakazawa, M. Uchiyama, K. Morokuma, T. Nagano, K. Hanaoka, Development of Azo-based fluorescent probes to detect different levels of hypoxia, Angew. Chem. Int. Ed. 52 (2013) 13028–13032.
[32] P. Verwilst, J. Han, J. Lee, S. Mun, H.G. Kang, J.S. Kim, Reconsidering azobenzene as a component of small-molecule hypoxia-mediated cancer drugs: a theranostic case study, Biomaterials 115 (2017) 104–114.
[33] M. Danaei, M. Dehghankhold, S. Ataei, F.H. Davarani, R. Javanmard, A. Dokhani, S. Khorasani, M.R. Mozafari, Impact of particle size and Polydispersity index on the clinical applications of Lipidic Nanocarrier systems, Pharmaceutics 10 (2018) 57.
[34] I.M. Adjei, B. Sharma, C. Peetla, V. Labhasetwar, Inhibition of bone loss with surface-modulated, drug-loaded nanoparticles in an intraosseous model of prostate cancer, J. Control. Release 232 (2016) 83–92.
[35] J. Panchal, J. Kotarek, E. Marszal, E.M. Topp, Analyzing subvisible particles in protein drug products: a comparison of dynamic light scattering (DLS) and resonant mass measurement (RMM), AAPS J. 16 (2014) 440–451.
[36] R.Z. Zhao, S. Jiang, N.Y. Ru, B. Jiao, Z.B. Yu, Comparison of hypoxic effects induced by chemical and physical hypoxia on cardiomyocytes, Can. J. Physiol. Pharmacol. 97 (2019) 980–988.
[37] L. Cavallini, M. Valente, A. Bindoli, NADH and NADPH inhibit lipid peroxidation promoted by hydroperoxides in rat liver microsomes, BBA-Lipid Lipid Met. 752 (1983) 339–345.
[38] T. Ito, L. Sun, M.A. Bevan, R.M. Crooks, Comparison of nanoparticle size and electrophoretic mobility measurements using a carbon-nanotube-based coulter counter, dynamic light scattering, transmission electron microscopy, and phase analysis light scattering, Langmuir 20 (2004) 6940–6945.
[39] T.T. Nguyen, D.P. Tran, P.D.Q. Huy, Z. Hoang, P. Carloni, P.V. Pham, C. Nguyen, M.S. Li, Ligand binding to anti-cancer target CD44 investigated by molecular simulations, J. Mol. Model. 22 (2016).
[40] T.K. Ryu, R.H. Kang, K.Y. Jeong, D.R. Jun, J.M. Koh, D. Kim, S.K. Bae, S.W. Choi, Bone-targeted delivery of nanodiamond-based drug carriers conjugated with alendronate for potential osteoporosis treatment, J. Control. Release 232 (2016) 152–160.
[41] E.A. Sheta, H. Trout, J.J. Gildea, M.A. Harding, D. Theodorescu, Cell density mediated pericellular hypoxia leads to induction of HIF-1α via nitric oxide and Ras/MAP kinase mediated signaling pathways, Oncogene 20 (2001) 7624–7634.
[42] V.P. Torchilin, Recent advances with liposomes as pharmaceutical carriers, Nat. Rev. Drug Discov. 4 (2005) 145–160.
[43] D. Manzanares, V. Ceña, Endocytosis: the nanoparticle and submicron nanocompounds gateway into the cell, Pharmaceutics 12 (2020) 371.
[44] A. Sukhanova, S. Bozrova, P. Sokolov, M. Berestovoy, A. Karaulov, I. Nabiev, Dependence of nanoparticle toxicity on their physical and chemical properties, Nanoscale Res. Lett. 13 (2018) 44.
[45] J.S. Suk, Q. Xu, N. Kim, J. Hanes, L.M. Ensign, PEGylation as a strategy for improving nanoparticle-based drug and gene delivery, Adv. Drug Deliv. Rev. 99 (2016) 28–51.
[46] F. Aielli, M. Ponzetti, N. Rucci, Bone metastasis pain, from the bench to the bedside, Int. J. Mol. Sci. 20 (2019) 280.
[47] A.J. Roelofs, K. Thompson, F.H. Ebetino, M.J. Rogers, F.P. Coxon, Bisphosphonates: molecular mechanisms of action and effects on bone cells, monocytes and macrophages, Curr. Pharm. Des. 16 (2010) 2950–2960.

[48] Y.F. He, Y.J. Huang, Z.Y. Huang, Y.L. Jiang, X.Q. Sun, Y.F. Shen, W.J. Chu, C. S. Zhao, Bisphosphonate-functionalized coordination polymer nanoparticles for the treatment of bone metastatic breast cancer, J. Control. Release 264 (2017) 76–88.
[49] L. Coenegrachts, C. Maes, S. Torrekens, R. Van Looveren, M. Mazzone, T.A. Guise, R. Bouillon, J.M. Stassen, P. Carmeliet, G. Carmeliet, Anti-placental growth factor reduces bone metastasis by blocking tumor cell engraftment and osteoclast differentiation, Cancer Res. 70 (2010) 6537–6547.
[50] D.I.H. Muller, C. Stoll, K. Palumbo-Zerr, C. Bohm, B. Krishnacoumar, N. Ipseiz, J. Taubmann, M. Zimmermann, M. Bottcher, D. Mougiakakos, J. Tuckermann, F. Djouad, G. Schett, C. Scholtysek, G. Kronke, PPAR delta-mediated mitochondrial rewiring of osteoblasts determines bone mass, Sci. Rep. 10 (2020) 8428.
[51] T. Ninomiya, A. Hosoya, H. Nakamura, K. Sano, T. Nishisaka, H. Ozawa, Increase of bone volume by a nanosecond pulsed laser irradiation is caused by a decreased osteoclast number and an activated osteoblasts, Bone 40 (2007) 140–148.
[52] M.N. Wang, F. Xia, Y.Q. Wei, X.W. Wei, Molecular mechanisms and clinical management of cancer bone metastasis, Bone Res. 8 (2020) 30.